Materials Chemistry and Physics 241 (2020) 122404

Contents lists available at ScienceDirect

Materials Chemistry and Physics

journal homepage: www.elsevier.com/locate/matchemphys

Microcontainer-based waterborne epoxy coatings for AA2024-T3: Effect of nature and number of polyelectrolyte multilayers on active protection performance

Inime Ime Udoh [a,b], Hongwei Shi [a,*], Fuchun Liu [a], En-Hou Han [a]

[a] CAS Key Laboratory of Nuclear Materials and Safety Assessment, Institute of Metal Research, Chinese Academy of Sciences, Shenyang, 110016, PR China
[b] University of Chinese Academy of Sciences, (UCAS), Shijingshan District, Beijing, 100049, PR China

HIGHLIGHTS

- Smart microcontainer-based water borne epoxy coating for anticorrosion protection of AA 2024-T3.
- New insights on effect of weak-strong and weak-weak polyelectrolyte multilayers on fabricated microcontainers.
- Polyelectrolyte multilayer-aided controlled active anticorrosion properties.

GRAPHICAL ABSTRACT

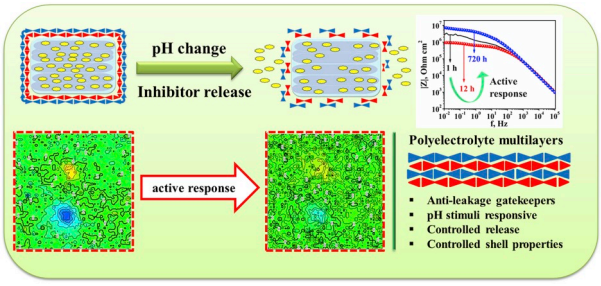

ARTICLE INFO

Keywords:
Aluminium alloy
Polyelectrolytes
Epoxy coating
EIS
Controlled release

ABSTRACT

New insights on the effect of nature and number of polyelectrolyte (PE) shells on active anticorrosion potential of microcontainers (MCs) applied as pH-sensitive reservoirs in coatings for the protection of AA2024-T3 is reported. Mesoporous silica particles (MSP) were loaded with benzotriazole (BTA) and shelled with different polyelectrolyte multilayers (PEM), demonstrating pH sensitivity. Weak-weak polyelectrolyte (W-W PE) shells allow immediate release of inhibitor, but weak-strong polyelectrolyte (W-S PE) shells encourage slower, more controlled and prolonged release, as revealed by release profiles of BTA from microcontainers. Active anticorrosion protection characterizations of the coatings doped with microcontainers were carried out by electrochemical techniques (EIS, SVET) and salt spray tests. Results reveal dependence of active properties of coatings on the nature and number of polyelectrolyte multilayers of microcontainers. We anticipate that proper choice of PEMs on smart containers can aid controlled functionalization of active feedback systems.

1. Introduction

Coatings have found wide application in the control of corrosion. Typically, the coating matrix creates a barrier and, thus avoids the contact of water and aggressive species with the metallic substrate. In the event where pores, cracks, delamination zones and blisters occur in the coating the barrier no longer holds, the inhibitor pigments or loaded inhibitors then slow corrosion activities on the surface of the metal offering an active protection. However, in most cases, direct addition of corrosion inhibitors interact with the coating formulation, and a

* Corresponding author.
E-mail address: hwshi@imr.ac.cn (H. Shi).

https://doi.org/10.1016/j.matchemphys.2019.122404
Received 5 July 2019; Received in revised form 1 October 2019; Accepted 3 November 2019
Available online 5 November 2019

Table 1
List of coating formulations.

Sample identification	% Additives	Description
Reference	0	Epoxy, without additives.
f-BTA	2 and 6 wt %	Epoxy + free benzotriazole (BTA)
BTA@MSP	2 and 6 wt %	Epoxy + BTA-loaded mesoporous silica particle (MSP)
BTA@MSP/PAH/PSS	2 and 6 wt %	Epoxy + BTA-loaded MSP, shelled with PAH/PSS
BTA@MSP/PEI/PAA	2 and 6 wt %	Epoxy + BTA-loaded MSP, shelled with PEI/PAA
BTA@MSP/2(PAH/PSS)	2 and 6 wt %	Epoxy + BTA-loaded MSP, shelled with PAH/PSS/PAH/PSS
BTA@MSP/2(PEI/PAA)	2 and 6 wt %	Epoxy + BTA-loaded MSP, shelled with PEI/PAA/PEI/PAA

deactivation of inhibitor together with (or) fast degradation of coating arise [1–7]. Therefore, to overcome these challenges the corrosion inhibitors are intercalated or encapsulated in micro or nanomaterials that have no detrimental interaction with the coating matrix, and dispersed in the coating formulation [8,9].

Smart coatings mitigate damages to coatings by offering rapid and sustained response to external impacts (e.g., cracks, pressure, and magnetic and electromagnetic fields) or to changes in the microenvironment (e.g., ion exchange and pH variation) [10,11]. Depending on the functionality of smart coatings, different systems can be engineered. However, due to local pH changes from redox activity accompanying onset and progression of corrosion on metal surfaces, pH-sensitive protective coatings are among the class of smart coatings significantly reported. Active protective coatings, as a class of smart coating, requires the ability of the coatings to respond with a release of active substances to repair damage caused by environmental changes over time [12]. Such coatings contain smart reservoirs with corrosion inhibitors pre-loaded [10,13]. Materials reported for this purpose include; halloysite clay nanotubes [14], calcium carbonate microbeads [15], hydroxyapatite

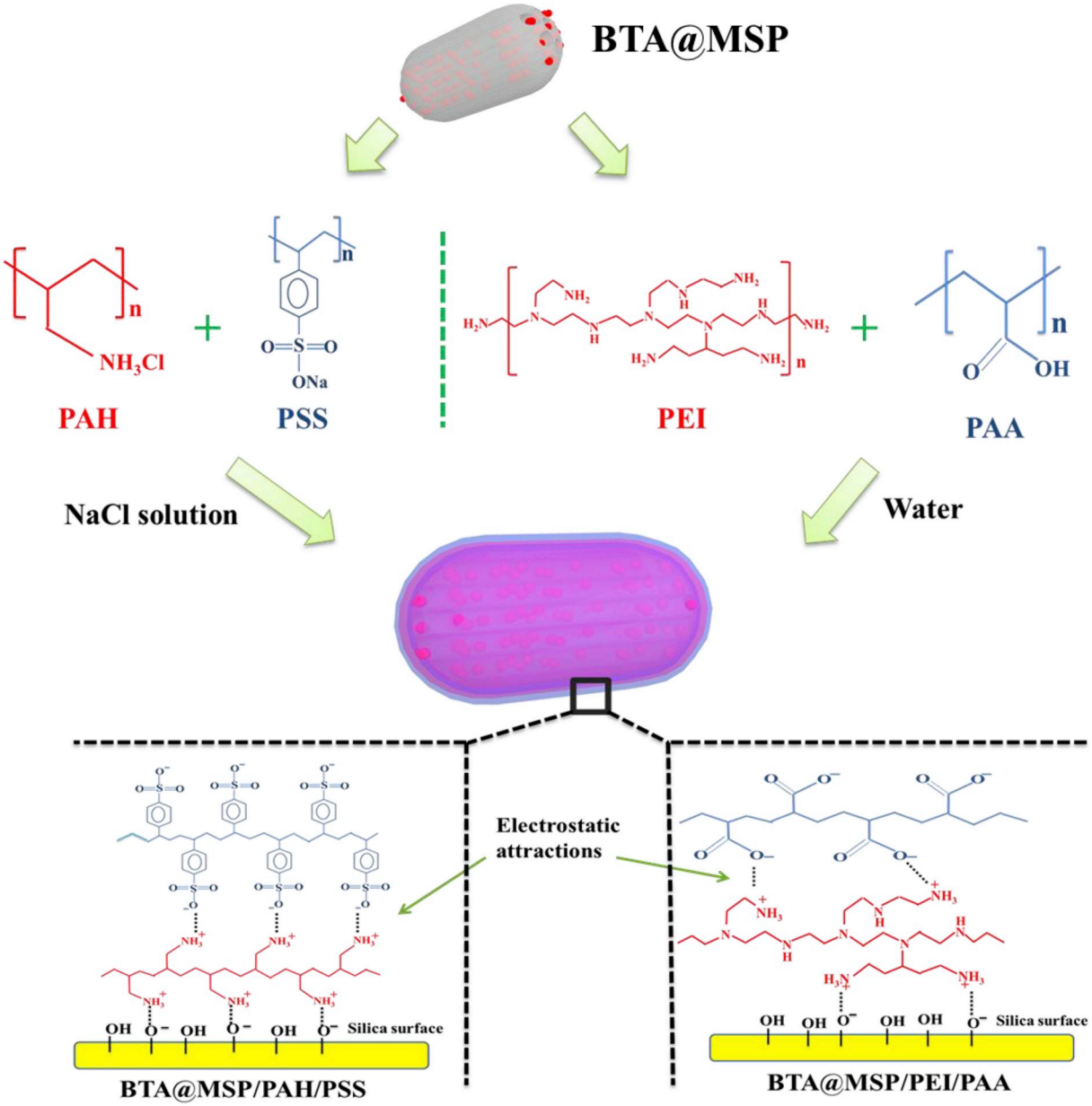

Fig. 1. Schematic illustration of the LbL polyelectrolyte deposition.

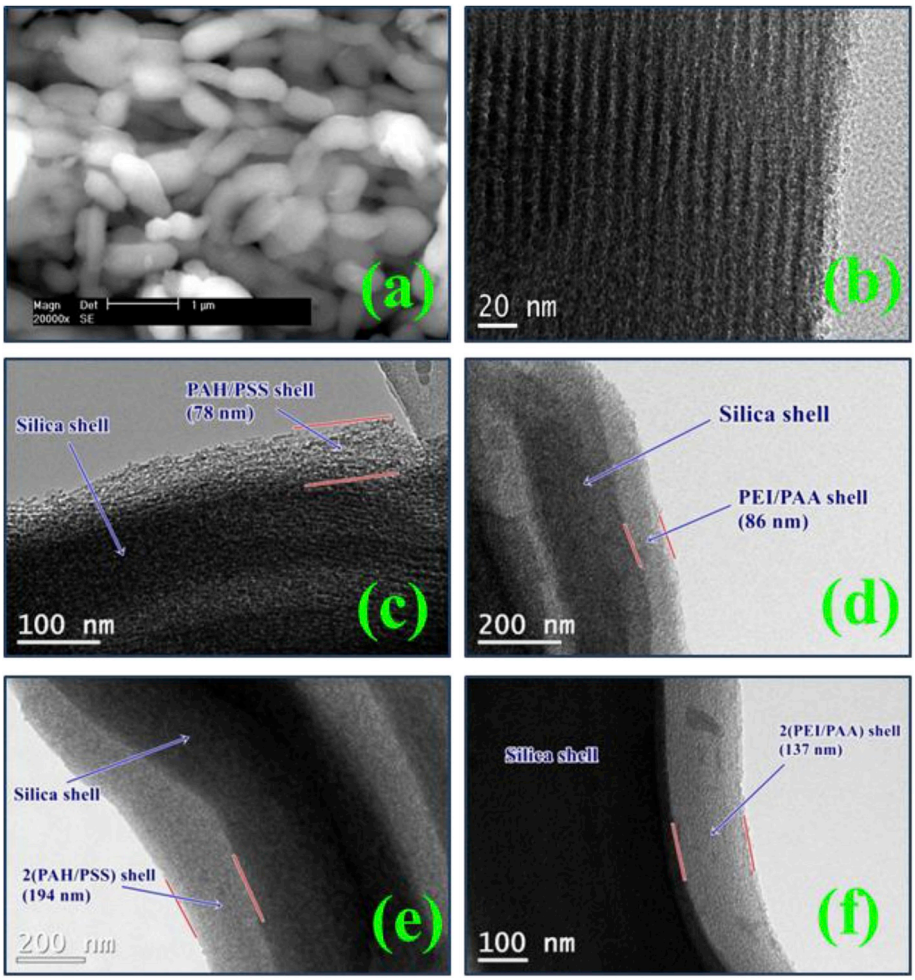

Fig. 2. SEM (a) and TEM (b) micrographs of as-received SBA mesoporous silica particles and TEM micrographs of microcontainers pre-loaded with BTA showing deposition of polyelectrolyte shells: (c) PAH/PSS, (d) PEI/PAA, (e) 2(PAH/PSS), and (f) 2(PEI/PAA).

microparticles [16], layered double hydroxide nanocontainers [17], titanates [18,19], carbon nanotubes [20], cellulose nanofibers [21], cerium molybdate containers [22], cobalt ferrite nanoparticles [23], ceramic nanocontainers [24] and polymeric particles [13,25].

However, common systems rely on pH-sensitive nano/micro particles or nano capsules, which release encapsulated active substances in a slow and prolonged manner when triggered to confer active protection [15,26–30]. Where microcontainers (MCs) are utilized, capping agents such as alternating layers of oppositely charged polyelectrolytes (PEs) can be deposited through a layer-by-layer (LbL) technique to prevent undesired leakage of encapsulated active substances, and to make the MCs stimuli-responsive, selectively permeable at different pH values and offer a controlled release of pre-loaded active substances upon change in environmental pH [31,32]. A number of authors have utilized polyelectrolyte multilayers (PEMs) as shells in the fabrication of containers for active feedback systems for preparation of anticorrosion protective coatings [2,27,28,33,34]. However, much work has not been carried out to examine the role the nature and number of PE layers play on the overall functionality of these containers.

In this work, we report a contribution to understanding the performance of smart coatings. The emphasis is on isolating the effect of the nature and number of PEMs used as shells for smart pH-responsive MCs, in order to examine their consequence on active protection capabilities of the coating. Focus is on the influence of weak-strong (W-S) and weak-weak (W-W) PE layers deposited on mesoporous silica particles (MSP) pre-loaded with benzotriazole (BTA) inhibitor, fabricated as smart pH-responsive reservoir in coatings for anticorrosion protection of aluminium alloy AA2024-T3. Strong PEs have a fixed charge due to strong anionic (e.g. $-SO_3^-$) or strong cationic (e.g. quaternary ammonium) groups. The charge on weak PEs is the result of the dissociation of weak acidic groups or the protonation of weak basic groups. Polyallylamine hydrochloride (PAH) and polystyrene sulfonate (PSS) pairs were utilized for the W-S PE combination, and polyethylene imine (PEI) and polyacrylic acid (PAA) solution was employed for the W-W PE layers. SBA-15, a type of commercially available MSP, served as an inorganic host to encapsulate organic inhibitors like BTA. Empty channels in a honeycomb-like ordered hexagonal porous structure, rigid framework, high stability and resistance to heat, mechanical stress and pH change, adequate pore volume and surface area, inner channels parallel to each other with openings at the two ends of the particles, are among the properties of SBA-15 which encourage hosting of inhibitors [32]. Literature provides evidence of the effectiveness of nitrogen-containing organic compounds as corrosion inhibitors for AA2024-T3, and BTA particularly demonstrating good inhibition, forming the basis for which BTA was chosen [35–39]. Morphological and structural characterizations of fabricated MCs were assisted by scanning electron microscopy (SEM), transmission electron microscopy (TEM), and Fourier transforms infrared (FTIR) spectroscopy. Zeta potential measurement was used to monitor successful deposition of oppositely charged PE layers on the silica surface. Encapsulation and release of BTA from MCs were assessed by UV–vis spectroscopy. Anticorrosion and active protection behaviour of coatings was evaluated by electrochemical measurements and SVET, together with further confirmation by salt spray tests.

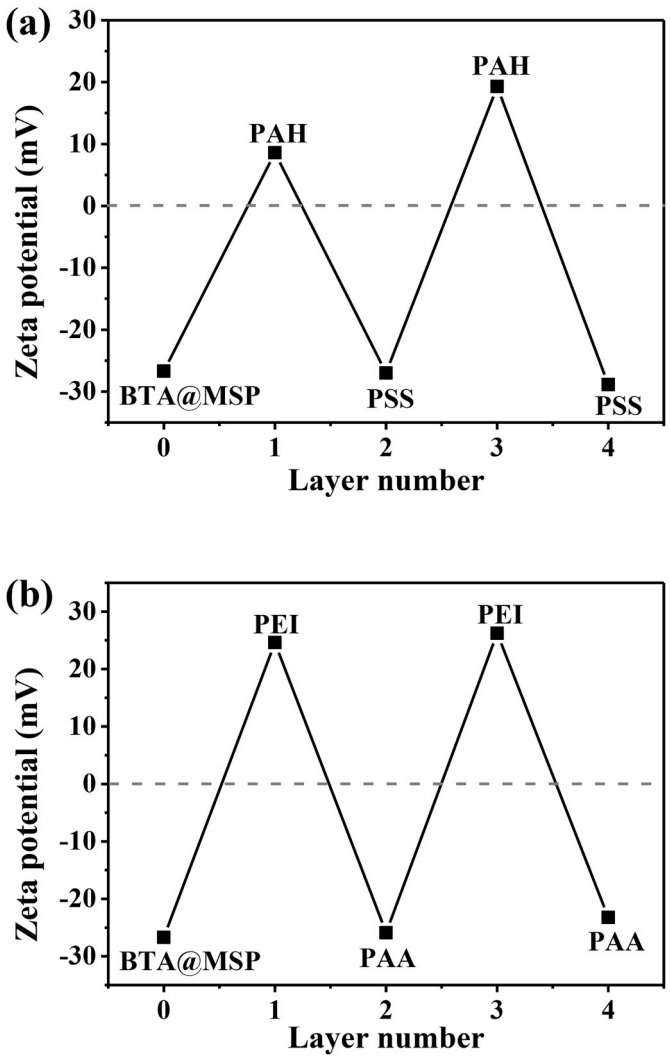

Fig. 3. Zeta potentials as a function of polyelectrolyte layer number alternatively coated with (a) PAH/PSS, and (b) PEI/PAA on MSP.

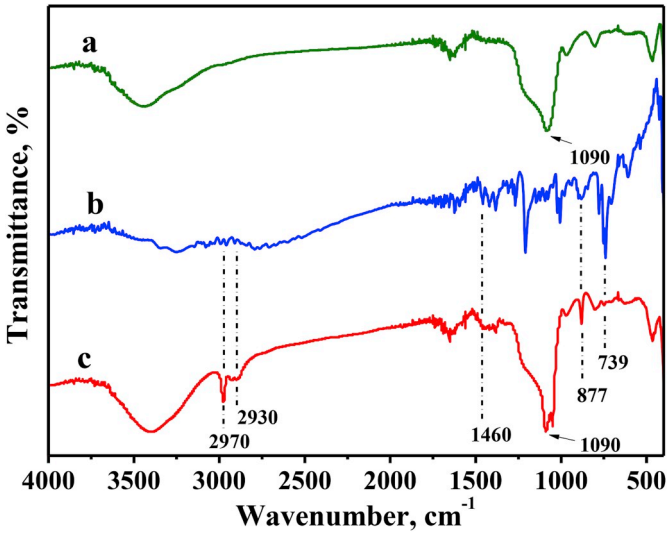

Fig. 4. FT-IR spectra of (a) MSP, (b) BTA and (c) BTA@MSP.

2. Experimental

2.1. Fabrication of pH sensitive microcontainers

Mesoporous silica particles, MSP (SBA-15) were supplied by XF Nano Materials Tech Co., Nanjing, China. The length and width of particles is from 0.5 to 1 μm and 0.2–0.5 μm, respectively. The mesochannels are of diameter 6–10 nm, and has specific surface area of 550–600 m^2/g. Polyallylamine hydrochloride (PAH, av. Mw ~58 000), poly-styrene sulphonate (PSS, av. Mw ~70,000), polyethyleneimine (PEI, av. Mw ~75,000), and poly (acrylic acid) solution (PAA, av. MW ~100 000, 35 wt% in H_2O) were purchased from Sigma-Aldrich. The corrosion inhibitor, benzotriazole (BTA) was purchased from Sinopharm Chemical Reagents (China). All reagents were analytical grade and used without further purification. Purified water was used to prepare solutions.

The mesochannels of MSP was impregnated with BTA (BTA@MSP) and monitored using UV–vis spectroscopy by the following procedure. First, dissolution of BTA in aqueous solution was carried out. MSP was added into the solution, dispersed and stirred for 30 min. To further ensure that BTA is properly sucked into the channels of MSP, the silica suspension in a beaker was placed in a vacuum pump and the air within the channels evacuated at room temperature. A repeat of the vacuum cycle for three times was carried out to ensure maximum loading. The silica suspension was then centrifuged to remove the excess BTA and recover particles, and dried. To determine the total amount of BTA loaded, BTA@MSP were dispersed in 0.1 M hydrofluoric acid solution for 3 h. Within the time, there was maximum release of BTA as silica particles dissolved. With a pipette, 1 mL of resulting solution was extracted, filtered, and the UV absorbance of BTA was measured at λ_{max} 258 nm. The concentration of BTA was obtained by extrapolating from a BTA calibration curve (correlation coefficient = 0.998) obtained in 0.1 M HF solution. The encapsulation efficiency was calculated using the expression in Eq. (1) [40]:

$$\%E = \frac{nBTAext}{nBTAini} \quad X \quad 100 \tag{1}$$

where nBTAext represents amount of BTA extracted from BTA@MSP and nBTAini is the initial amount of BTA used in the loading step.

In order to obtain microcontainers with polyelectrolyte shell around the MSP surface, the LbL deposition procedure was followed. For MCs with W-S PE (PAH/PSS) shell, the deposition of positive PAH was performed by adding PAH (6 mg mL^{-1} in 0.5 M NaCl, 3 mL) to a BTA-saturated suspension of BTA-loaded MSPs (15 wt%, 20 mL, pH 7.5). The use of BTA-saturated solution to gently disperse BTA-loaded MSPs prevents free leakage of BTA during polyelectrolyte deposition procedure. The mixture was gently stirred at room temperature, and then allowed to stand still for about 20 min. Then, the BTA@MSP/PAH sample was subjected to washing, redispersion, and centrifugation in 0.05 M NaCl for three times. The washing/redispersion/centrifugation procedure was performed after each deposition step. Then the deposition of negative PSS layer was carried out by mixing PSS (6 mg mL^{-1} in 0.5 M NaCl, 3 mL) with the centrifuged BTA@MSP/PAH. The procedure was repeated with resulting MCs having the structure: BTA@MSP/PAH/PSS and BTA@MSP/2(PAH/PSS). For MCs with weak-weak polyelectrolyte (PEI/PAA) shell, the deposition of positive PEI was performed by adding PEI (6 mg mL^{-1} in water, 3 mL) to a suspension of BTA-loaded MSPs (15 wt%, 20 mL, pH 7.5). The mixture was subjected to the same treatment as with the first MC, but with washing/redispersion/centrifugation procedure carried out in purified water. The deposition of negative PAA layer (from 6 mg mL^{-1} in water, 3 mL) was then carried out. The procedure was repeated to obtain MCs with the structure: BTA@MSP/PEI/PAA and BTA@MSP/2(PEI/PAA). The successful formation of oppositely charged layers was confirmed by zeta-potential measurements. All samples were dried and ready for use.

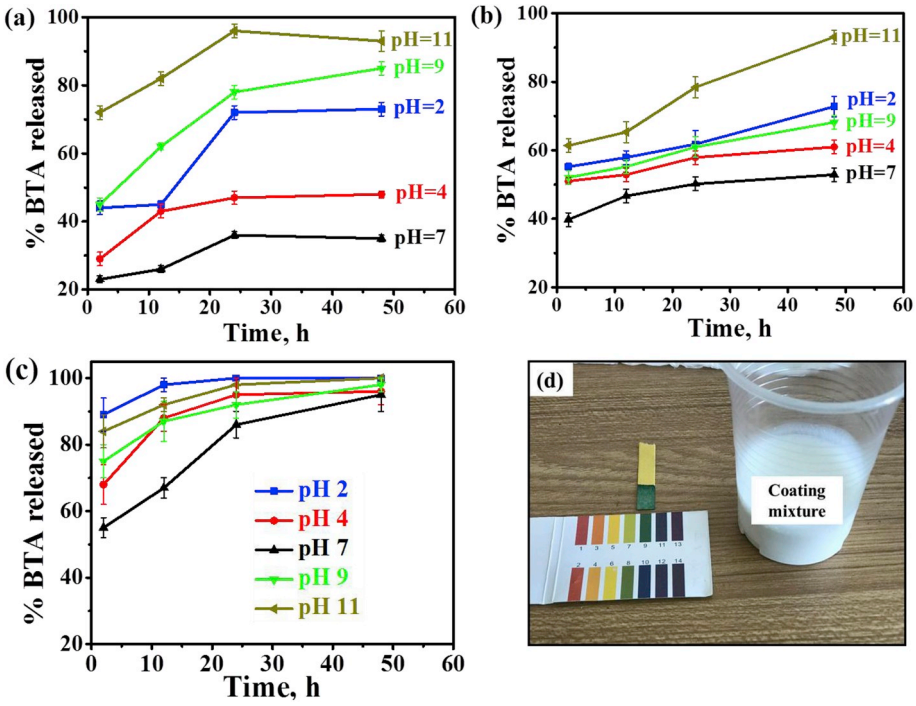

Fig. 5. Release profile of BTA from (a) BTA@MSP/(PAH/PSS)$_2$, (b) BTA@MSP/(PEI/PAA)$_2$, and (c) BTA@MSP in 0.5 M NaCl at different pH values. (d) illustration of the pH of coating mixture.

2.2. Characterization of microcontainers

The successful growth of positive and negative PE layers on MSPs was monitored using the Zetasizer (Nano-ZS90, Malvern Instruments, UK). Triplicate measurements at room temperature were taken at different stages of fabrication of MCs beginning with the silica shell to the last PE layer. At the loading stage, with the aid of a fourier transform infrared spectra (FT-IR), performed using a Nicolet 470 spectrometer from Brucker with KBr pellets, the functional groups and structure of the prepared MSP-BTA was characterized. The spectra were recorded between 500 and 4000 cm^{-1} with 1 cm^{-1} resolution in transmission mode. UV–vis spectroscopy was used to obtain the percentage amount of encapsulated BTA in the MC. The morphology of MCs and deposited PE shells were observed by scanning electronic microscope (SEM) and transmission electron microscopy (TEM). A XL30 type SEM from Philips was used for SEM observations, and a Jeol JEM 2010F TEM was employed for TEM observations.

2.3. Release studies of BTA from microcontainers

The release of BTA from MCs when exposed to 0.5 M NaCl at different pH values was examined using UV–vis spectroscopy at $\lambda_{max} = 258$ nm. Solutions of HCl and NaOH were used to adjust the pH and the release profiles were obtained for pH values 2, 4, 7, 9 and 11. Briefly, MCs (0.8 g) pre-encapsulated with BTA were dispersed in solution (80 mL). At different times of measurement, the solution was homogenized and an aliquot of 20 mL extracted with the help of a syringe, filtered, then the absorbance of BTA measured using the UV spectrophotometer. The concentration of released BTA in the solution was obtained by extrapolating from a BTA calibration curve, and the release percentage calculated. The release percentage was obtained after 2 h, 12 h, 24 h and 48 h incubation time.

2.4. Anticorrosion evaluation of microcontainers in coated AA2024-T3

Aluminium alloy 2024-T3 was purchased from Q-lab Corporation, USA, having a chemical composition (wt%): Si 0.06%, Fe 0.17%, Cu 4.54%, Mn 0.63%, Mg 1.51%, Cr 0.01%, Zn 0.08%, Ti 0.03% and Al balance. The bare AA2024-T3 substrates were first prepared following the procedure described elsewhere [41]. Water-borne epoxy coating was used in this work. A commercial 620 epoxy resin and 703 polyamide resin hardener supplied by Shanghai Resin Company, China, were used in this work. Using high-speed dispersion machine, epoxy resin was mixed (1200 revolutions per min for 30 min) with different MCs and at different percentage concentrations, which was subsequent upon curing with polyamide resin. Different coatings were obtained by incorporating (2 wt% and 6 wt% with respect to the resin) of MCs into the resin. A uniform dispersion was obtained after stirring for 30 min. A reference sample was also prepared without MCs by the mixture of epoxy resin with polyamide resin at the ratio 2.5:1. Table 1 gives the list of the coating formulations. The application of coatings on AA2024-T3 substrate was by air spraying (30 ± 2 μm thicknesses). Prepared samples were left to dry at room temperature for up to 168 h before tests.

Electrochemical impedance spectroscopy (EIS) measurements were carried out at room temperature to study the barrier effect of MCs on coated AA2024-T3 immersed in 0.1 M NaCl solutions (V = 50 mL, stagnant and in equilibrium with air). The electrode cell consisted of a saturated calomel reference electrode (SCE), a platinum foil counter electrode and an AA2024-T3 plate placed in horizontal position with an exposed area of 12.56 cm^2 serving as the working electrode. Before measurements, the electrochemical cell was placed in a Faraday cage to avoid the interference of external electromagnetic fields. All measurements were performed using Gamry 600+ Potentiostat/Galvanostat/ZRA connected to a computer. EIS measurements were preceded by an open circuit delay for 20 min. The Gamry Echem Analyst 7.05 software was used to fit data. Measurements were made over a frequency range from 100 kHz to 10 mHz with 20 mV sinusoidal perturbations.

Scanning vibrating electrode technique (SVET) measurements were taken using SVET equipment. The equipment is supplied by Applicable Electronics and controlled by Sciencewares ASET program. Aided by a metallic needle, two artificial defects were made on each coated sample by drilling to penetrate the epoxy coating completely prior to the measurement. An area of about 10 mm^2 (3.2 mm × 3.1 mm) of samples was exposed to corrosive solution. Measurements proceeded with Pt-Ir

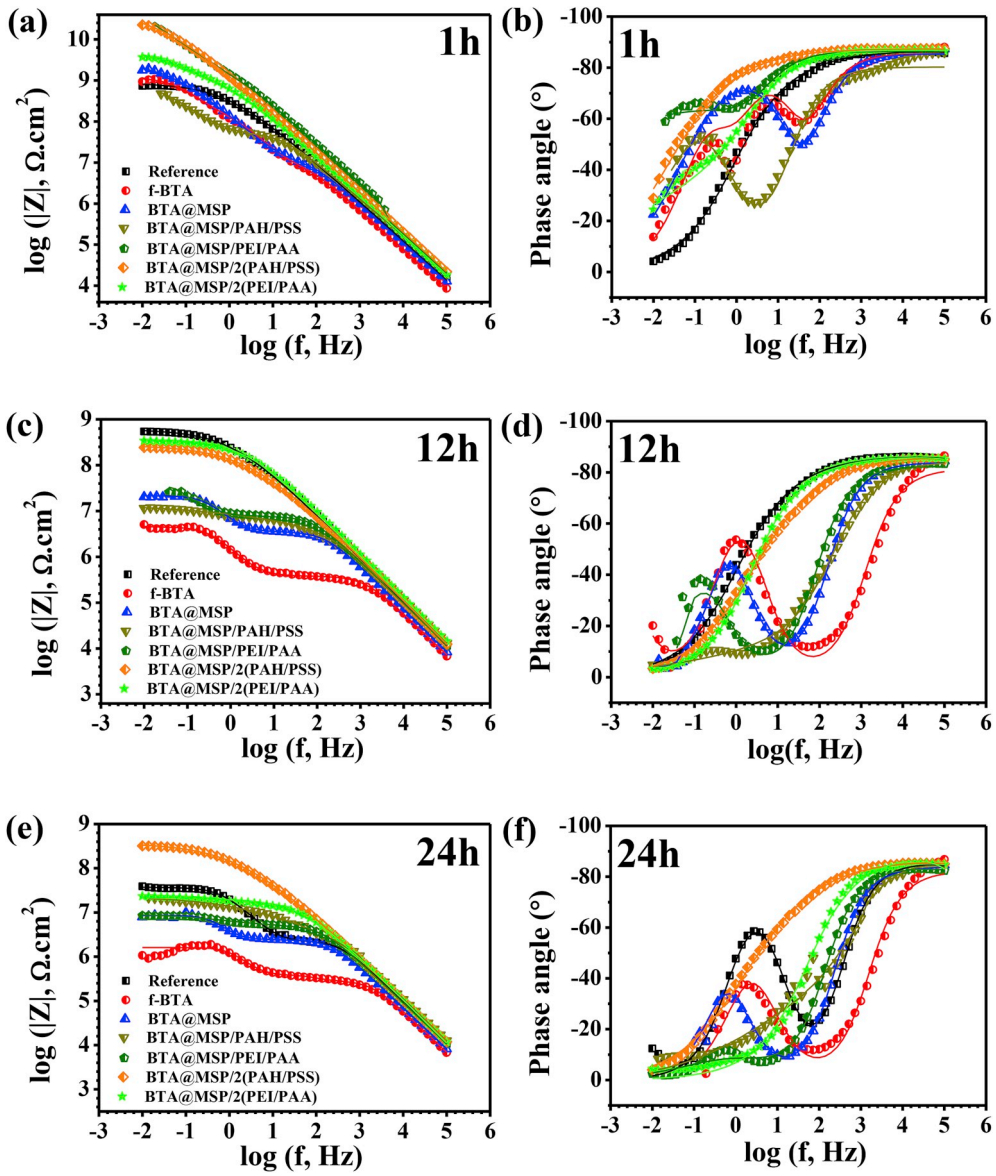

Fig. 6. Bode plots of behaviour of coated aluminium alloy 2024-T3 immersed in 0.1 M NaCl solution in the absence and presence of 2 wt% microcontainers after (a, b) 1 h, (c, d) 12 h, (e, f) 24 h, (g, h) 144 h, and (i, j) 720 h. Symbols show data. Lines represent fitting.

probes platinized to obtain a 30 μm diameter ball of platinum at the tip. Measurements were taken in 0.05 M NaCl solution at open circuit potential, at a frequency of probe vibration (325 Hz) direction perpendicular to sample surface. The acquisition time for each data point was 0.6 s and map of local ionic densities were obtained (2500 grid points). Detection of current densities was at 150 μm above the sample surface and data visualized using QuikGrid software.

Salt spray tests (SST) was performed following the ASTM B117 standard. In order to induce corrosion and carry out the test, long scratches were made on the coated samples using a sharp tool and exposed to 5% NaCl solution at 35 ± 2 °C. During examinations, samples were washed and dried, then observed within 30 min after removal from the salt spray chamber.

3. Results and discussion

3.1. Fabrication, morphology and composition of microcontainers

A schematic representation of the LbL deposition process of PEMs of fabricated MCs is given in Fig. 1. The LbL deposition of PEs is made possible by the electrostatic interactions between protonated amino groups (cationic) and sulfonate groups (anionic) of PAH and PSS, respectively [42,43]. A similar interaction is obtained for protonated amine groups and dissociated carboxylic acid groups of PEI and PAA, respectively [44]. Silanol (Si-OH) groups on the silica surface that are deprotonated allow for electrostatic interaction with the first layer of cationic PE [45], after which other PE layers are successively deposited.

The SEM and TEM micrographs of as-received MSP are shown in Fig. 2a and b, respectively. It can be seen from Fig. 2a that MSP has slightly curved rectangular shapes with oval edges. The particles have sub-micrometer sizes. The inner meso-channels and silica shell of MSP without PEs are revealed in Fig. 2b. Fig. 2c–f show PE shell deposited on mesoporous silica corresponding to PAH/PSS, PEI/PAA, 2(PAH/PSS) and 2(PEI/PAA) single and double pairs of PEs, respectively. A range of PE shell thickness is observed on the silica surface. From Fig. 2c and d, an estimated shell thickness of about 78 nm and 86 nm is observed for single PE PAH/PSS and PEI/PAA shells, respectively. However, double layers of PE pairs (see Fig. 2e and f) reveal thicker shells of about 194 nm

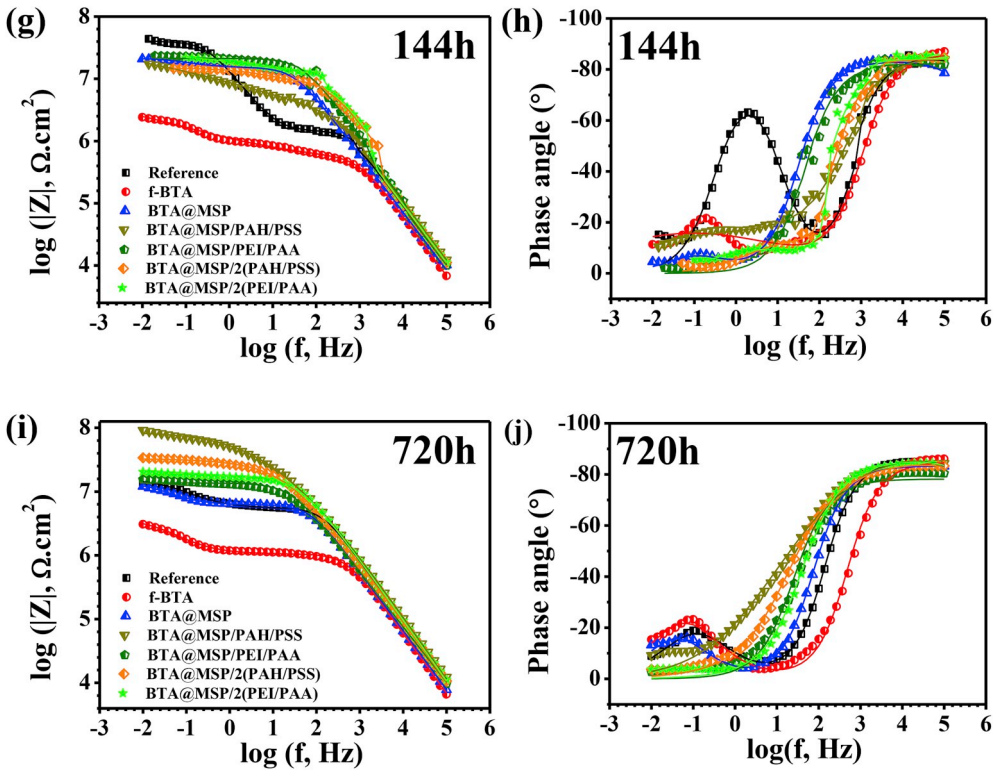

Fig. 6. (*continued*).

and 137 nm for 2(PAH/PSS) and 2(PEI/PAA) shells, respectively. Addition of more PE layers to MCs increases the size of MCs which is due to the growth of PE shells [5].

The successful deposition of PEs on silica shell is confirmed by zeta potential measurements as shown in Fig. 3a and b. The initial MSP loaded with BTA has a negative zeta potential of −26.7 mV. For W-S PAH/PSS layers (Fig. 3a), a change from negative zeta potential to positive (8.6 mV) is observed upon deposition of PAH, a polycation. Furthermore, a layer of PSS polyanion added moves the potential again to negative (−27 mV). Further depositions of PAH and PSS layers alternates the zeta potential to 19.3 mV and −28.9 mV, respectively. A similar trend of alternating zeta potential is observed for W-W PEI/PAA layers (Fig. 3b). For MCs with both PAH/PSS and PEI/PAA layers, the alternating zeta potential in the positive and negative directions indicates successful deposition of the PE layers [46].

The FT-IR spectra of as-received MSP, BTA, and BTA loaded MSP (BTA@MSP) are presented in Fig. 4. The characteristic peaks representing the different functional groups present are identified. The spectra for both MSP and BTA@MSP (Fig. 4a and c) show characteristic MSP peak at 1090 cm^{-1}, corresponding to stretching vibration Si-O-Si bonds [39]. The spectrum of BTA@MSP also has peaks that are characteristic of functional groups in BTA which are shown in Fig. 4b (broken lines guide the eye). The spectra reveal peaks at 739 cm^{-1} and 877 cm^{-1} attributed to C-H out of plane bending. The peak at 1460 cm^{-1} is assigned to C-N stretching vibration [47]. Peaks at 2930 cm^{-1} and 2970 cm^{-1} can be attributed to C-H asymmetric stretch [48]. The presence of functional groups of the inhibitor BTA in the spectrum of BTA@MSP indicates successful loading into MSP.

3.2. Profiles of BTA release from microcontainers

The onset of corrosion is usually triggered by aggressive anion present in the solution. It is expected that upon the onset of corrosion a good inhibitor pre-loaded in an inorganic micro or nanocontainer present in the organic coating is released to consequently impede or slow down corrosion activity, and maintain the integrity of the coating by active protection abilities. To achieve this, the container limits the release of the inhibitor in the neutral pH of the environment, and encourages release of same upon demand when the pH changes towards the acidic and alkaline regions. Corrosion activity of AA2024-T3 when exposed to neutral NaCl solutions is accompanied by a change in the local pH arising from anodic and cathodic reactions [32]. The PE shells of the microcontainers acting as "gate keepers" open and close in response to the local pH changes. It is the ability of the microcontainers to release inhibitors in acidic and alkaline pH environments and to control spontaneous leakage of same in neutral pH that makes it a functional component of smart coatings, for the release of inhibitor on demand. From UV spectroscopy data, the amount of BTA in BTA@MSP obtained in this work is 66 mg g^{-1} of initial amount of MSP, corresponding to 5.5%. With this amount, the impedance of corrosion activity can be effectively studied if MCs can release on demand [49], although it can be optimized.

PE layers that are mainly based on electrostatic interactions, particularly for single pairs, can be unstable in the presence of water [50]. Therefore, a more stable release profile obtained for BTA from MCs with W-S [2(PAH/PSS)] and W-W [2(PEI/PAA)] double pairs of PE layer shells is presented in Fig. 5a and b. The release of BTA from MCs dispersed in 0.5 M NaCl solutions at different pH conditions (2, 4, 7, 9 and 11) was monitored by UV–vis spectroscopy. From the profiles at different pH values, similar shapes are obtained but with difference in the amount of BTA released. Release of BTA in the first 2 h is likely coming from the region of the MCs close to the shell and as time progresses BTA from the inner core is released [40]. MCs with W-W PE shells show higher release percentage in the first 2 h (Fig. 5b) in pH 2, 4, 7 and 9 solutions when compared with MCs with W-S PE shell (Fig. 5a). This could be explained in terms of the molecular structure of the PEMs. The molecular structure of PE used can confer different physicochemical properties on PEMs. For instance, growth of PEM films can either be linear or exponential [51]. It was reported by Lavelle and co-workers that linearly growing PE films have thicknesses increasing linearly

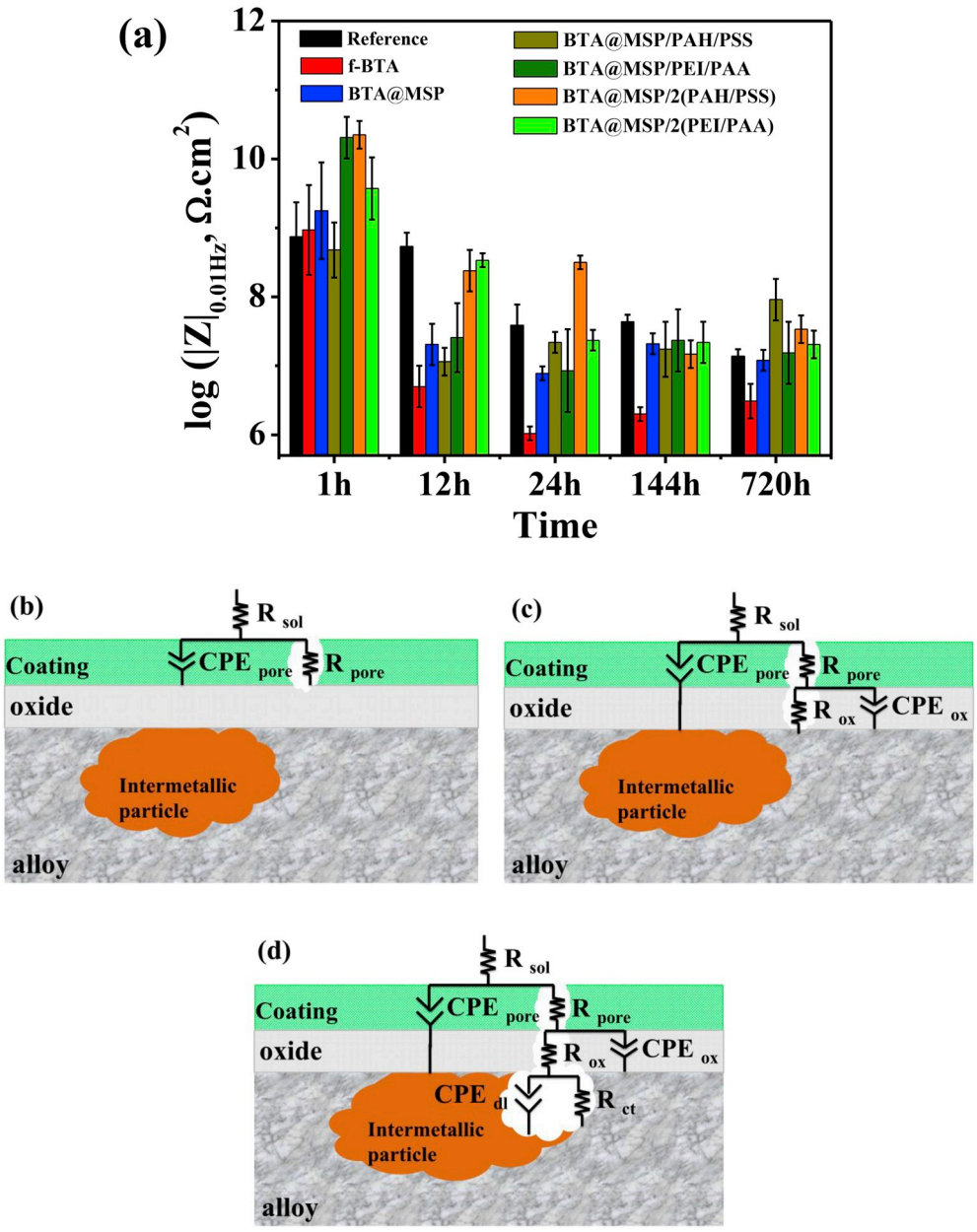

Fig. 7. (a) Evolution of lowest frequency impedance from EIS data of coated AA2024-T3 samples immersed in 0.1 M NaCl in the absence and presence of 2 wt% microcontainers; equivalent circuit used in fitting EIS data of coated AA2024-T3 samples with one time constant (b), two time constants (c), and three time constants (d).

with the number of deposition steps, and for the others, the thickness increases exponentially, at least for the first deposition step [52]. This could explain, amongst other factors, why the thickness of the SP layer of PEI/PAA is higher than PAH/PSS (Fig. 2c and d). However, citing the example of PAH/PSS films, Seon et al. and Laugel et al. explain that linearly growing PEM films are obtained for PE that interact strongly at each deposition step [51,53]. For such, the architecture of the PEM is stratified with no diffusion of PEs in the layers perpendicular to the film [54]. For exponential growing PEM films, notably from a build-up between polycations and polyanions that interact weakly [53], for example PEI/PAA, such PEM films are much more hydrated and softer than linear ones [55]. Therefore, W-W PEI/PAA encourages more permeation of solution in the early hours through the PEM layers and release of BTA when compared with PAH/PSS.

The permeation of solution leads to multilayer swelling and thinning associated with PE layers [56], and with weaker electrostatic attractions 2(PEI/PAA) swell more than 2(PAH/PSS) in the first 2 h. As time progresses from 12 h to 48 h, a slower release is observed for 2(PEI/PAA). However, for 2(PAH/PSS), with layers that interact strongly, there is more resistance to penetration of solution, leading to a slower release of BTA in the first 2 h. The consequence is a gradual and more controlled release of BTA up to 48 h as observed in Fig. 5a. At high pH 11, both MCs show significantly high release of BTA. From the profiles, both MCs respond with a higher release of BTA upon changes in pH to acidic and alkaline regions, owing to variations in the solubility of BTA with pH. The analysis of release profile (Fig. 5) indicates the dependence of BTA inhibitor release on pH, which confirms the stimuli-responsive triggering of the MCs, and highlights the role of PE shells in the release behaviour. Hence, their suitability as components of smart coating based on pH triggering is confirmed. However, W-W PE shells seem to be more suitable for systems where immediate release of large amounts of active substances is expected. Furthermore, in the absence of PE shells,

Table 2
Parameters obtained from fitting EIS data for coated AA2024-T3; reference coating, and coating modified with 2 wt% f-BTA and BTA@MSP.

Time (h)	CPE_{pore} (S s^{-n} cm^{-2})	n_{pore}	R_{pore} (Ω cm^2)	CPE_{ox} (S s^{-n} cm^{-2})	n_{ox}	R_{ox} (Ω cm^2)	CPE_{dl} (S s^{-n} cm^{-2})	n_{dl}	R_{ct} (Ω cm^2)	Chi-squared
Reference										
1	$1.92 \pm 0.29 \times 10^{-10}$	0.96	$8.92 \pm 0.45 \times 10^{8}$							1.49×10^{-3}
12	$2.29 \pm 0.11 \times 10^{-10}$	0.96	$6.19 \pm 0.21 \times 10^{8}$							1.07×10^{-3}
24	$2.88 \pm 0.53 \times 10^{-10}$	0.95	$2.3 \pm 0.33 \times 10^{6}$	$6.32 \pm 0.34 \times 10^{-9}$	0.97	$3.55 \pm 0.27 \times 10^{7}$				2.56×10^{-3}
144	$3.11 \pm 0.16 \times 10^{-10}$	0.95	$1.48 \pm 0.22 \times 10^{6}$	$1.8 \pm 0.12 \times 10^{-8}$	0.92	$3.9 \pm 0.44 \times 10^{7}$				4.39×10^{-3}
720	$2.89 \pm 0.27 \times 10^{-10}$	0.95	$5.56 \pm 0.19 \times 10^{6}$	$2 \pm 0.15 \times 10^{-7}$	0.69	$1.03 \pm 0.28 \times 10^{7}$				2.22×10^{-4}
f-BTA										
1	$3.52 \pm 0.38 \times 10^{-10}$	0.95	$1.21 \pm 0.18 \times 10^{7}$	$6.68 \pm 0.41 \times 10^{-10}$	0.94	$2.31 \pm 0.15 \times 10^{8}$	$1.3 \pm 0.12 \times 10^{-9}$	1	$1.01 \pm 0.22 \times 10^{9}$	1.37×10^{-2}
12	$7.91 \pm 0.19 \times 10^{-10}$	0.9	$3.83 \pm 0.14 \times 10^{5}$	$1.23 \pm 0.21 \times 10^{-7}$	0.94	$4.15 \pm 0.19 \times 10^{6}$	$1.38 \pm 0.1 \times 10^{-5}$	1	$9.08 \pm 0.14 \times 10^{8}$	1×10^{-2}
24	$5.29 \pm 0.18 \times 10^{-10}$	0.94	$2.9 \pm 0.31 \times 10^{5}$	$1.67 \pm 0.15 \times 10^{-8}$	0.99	$1.23 \pm 0.12 \times 10^{5}$	$1.01 \pm 0.2 \times 10^{-7}$	1	$1.17 \pm 0.19 \times 10^{6}$	4.13×10^{-2}
144	$4.09 \pm 0.33 \times 10^{-10}$	0.96	$4.94 \pm 0.26 \times 10^{5}$	$7.69 \pm 0.32 \times 10^{-7}$	0.32	$5.26 \pm 0.22 \times 10^{6}$				4.64×10^{-3}
720	$4.94 \pm 0.17 \times 10^{-10}$	0.94	$1.05 \pm 0.12 \times 10^{6}$	$1.27 \pm 0.12 \times 10^{-6}$	0.69	$2.86 \pm 0.23 \times 10^{6}$				2.42×10^{-3}
BTA@MSP										
1	$2.35 \pm 0.26 \times 10^{-10}$	0.95	$1.15 \pm 0.19 \times 10^{7}$	$1.38 \pm 0.12 \times 10^{-9}$	0.82	$2.16 \pm 0.11 \times 10^{9}$				2.4×10^{-3}
12	$5.85 \pm 0.19\ 10^{-10}$	0.63	$1.01 \pm 0.1 \times 10^{2}$	$3.62 \pm 0.18 \times 10^{-10}$	0.95	$3.63 \pm 0.2 \times 10^{6}$	$3.25 \pm 0.13 \times 10^{-8}$	0.96	$1.79 \pm 0.13 \times 10^{7}$	1.37×10^{-3}
24	$4.8 \pm 0.22 \times 10^{-10}$	0.93	$2.4 \pm 0.31 \times 10^{6}$	$4.49 \pm 0.22 \times 10^{-8}$	1	$7.18 \pm 0.24 \times 10^{5}$	$2.43 \pm 0.21 \times 10^{-8}$	1	$5.56 \pm 0.22 \times 10^{6}$	1.13×10^{-2}
144	$4.9 \pm 0.18 \times 10^{-10}$	0.93	$1.53 \pm 0.19 \times 10^{7}$	$2.42 \pm 0.22 \times 10^{-7}$	0.74	$6.38 \pm 0.22 \times 10^{6}$				1.32×10^{-3}
720	$5.46 \pm 0.12 \times 10^{-10}$	0.93	$6.2 \pm 0.22 \times 10^{6}$	$5.05 \pm 0.25 \times 10^{-7}$	0.74	$8.14 \pm 0.19 \times 10^{6}$				2.49×10^{-4}

Table 3
Parameters obtained from fitting EIS data for coated AA2024-T3; coatings modified with 2 wt% BTA@MSP/PAH/PSS, BTA@MSP/PEI/PAA, BTA@MSP/2(PAH/PSS) and BTA@MSP/2(PEI/PAA).

Time (h)	CPE_{pore} (S s^{-n} cm^{-2})	n_{pore}	R_{pore} (Ω cm^2)	CPE_{ox} (S s^{-n} cm^{-2})	n_{ox}	R_{ox} (Ω cm^2)	Chi-squared
BTA@MSP/PAH/PSS							
1	$2.22 \pm 0.23 \times 10^{-10}$	0.95	$9.16 \pm 0.22 \times 10^{5}$	$2.54 \pm 0.31 \times 10^{-8}$	0.33	$6.29 \pm 0.23 \times 10^{7}$	5.39×10^{-3}
12	$2.37 \pm 0.17 \times 10^{-10}$	0.95	$9.59 \pm 0.12 \times 10^{5}$	$2.12 \pm 0.14 \times 10^{-8}$	0.3	$1.22 \pm 0.11 \times 10^{7}$	1.84×10^{-4}
24	$2.07 \pm 0.11 \times 10^{-10}$	0.96	$7.17 \pm 0.52 \times 10^{5}$	$1.97 \pm 0.22 \times 10^{-8}$	0.4	$2.23 \pm 0.11 \times 10^{7}$	3.19×10^{-3}
144	$2.72 \pm 0.12 \times 10^{-10}$	0.94	$8.3 \pm 0.33 \times 10^{5}$	$6.9 \pm 0.22 \times 10^{-8}$	0.3	$3.82 \pm 0.23 \times 10^{7}$	1.65×10^{-3}
720	$1.59 \pm 0.12 \times 10^{-10}$	0.99	$8.64 \pm 0.45 \times 10^{7}$				4.21×10^{-3}
BTA@MSP/PEI/PAA							
1	$1.35 \pm 0.15 \times 10^{-10}$	0.96	$1.13 \pm 0.12 \times 10^{9}$	$2.22 \pm 0.21 \times 10^{-10}$	0.65	$7.46 \pm 0.49 \times 10^{11}$	1.16×10^{-3}
12	$4.27 \pm 0.21 \times 10^{-10}$	0.91	$7.69 \pm 0.3 \times 10^{6}$	$6.53 \pm 0.11 \times 10^{-8}$	0.91	$2.93 \pm 0.13 \times 10^{7}$	6.27 ×10-3
24	$4.24 \pm 0.22 \times 10^{-10}$	0.92	$5.18 \pm 0.33 \times 10^{6}$	$1.19 \pm 0.15 \times 10^{-7}$	0.84	$3.34 \pm 0.22 \times 10^{6}$	4.19×10^{-4}
144	$3.26 \pm 0.12 \times 10^{-10}$	0.95	$2.27 \pm 0.22 \times 10^{7}$				2.37×10^{-3}
720	$9 \pm 0.13 \times 10^{-10}$	0.87	$1.37 \pm 0.27 \times 10^{7}$				7.05×10^{-3}
BTA@MSP/2(PAH/PSS)							
1	$1.08 \pm 0.11 \times 10^{-10}$	0.97	$5.16 \pm 0.22 \times 10^{10}$				5.48×10^{-4}
12	$2.14 \pm 0.22 \times 10^{-10}$	0.96	$2.72 \pm 0.17 \times 10^{8}$				7.22×10^{-4}
24	$2.27 \pm 0.15 \times 10^{-10}$	0.96	$3.68 \pm 0.33 \times 10^{8}$				7.33×10^{-4}
144	$3.51 \pm 0.24 \times 10^{-10}$	0.93	$8.14 \pm 0.29 \times 10^{6}$	$4.14 \pm 0.22 \times 10^{-8}$	0.62	$6.81 \pm 0.22 \times 10^{6}$	3.82×10^{-3}
720	$2.83 \pm 0.17 \times 10^{-10}$	0.95	$3.29 \pm 0.23 \times 10^{7}$				7.58×10^{-4}
BTA@MSP/2(PEI/PAA)							
1	$1.39 \pm 0.13 \times 10^{-10}$	0.97	$1.67 \pm 0.11 \times 10^{8}$	$5.22 \pm 0.33 \times 10^{-10}$	0.4	$1.25 \pm 0.22 \times 10^{10}$	1.25×10^{-3}
12	$1.87 \pm 0.2 \times 10^{-10}$	0.96	$3.55 \pm 0.11 \times 10^{8}$				8.18×10^{-5}
24	$1.47 \pm 0.12 \times 10^{-10}$	0.99	$2.17 \pm 0.33 \times 10^{7}$				3.46×10^{-3}
144	$3.23 \pm 0.16 \times 10^{-10}$	0.94	$1.23 \pm 0.19 \times 10^{7}$	$8.18 \pm 0.26 \times 10^{-8}$	0.72	$9.53 \pm 0.17 \times 10^{6}$	1.71×10^{-3}
720	$2.5 \pm 0.22 \times 10^{-10}$	0.96	$1.88 \pm 0.16 \times 10^{7}$				2.07×10^{-3}

excessive premature leakage is observed as demonstrated in Fig. 5c, validating the importance of gatekeepers and capping materials for smart containers. However, it is important to note that the behaviour of MCs in water may be different from their behaviour in coating due to changes in environmental conditions. As indicated in Fig. 5d, the pH of the coating mixture is slightly alkaline; greater than 8, but less than 9. At this pH only a little amount of BTA might be released during coating fabrication. Therefore, greater fraction of BTA retained within MCs respond on demand when the pH is significantly reduced or increased upon onset of corrosion.

3.3. EIS assessment of anticorrosion efficiency of microcontainers in coated AA2024-T3

EIS is an important technique in the assessment of barrier and active protection properties of smart coatings applied on metals [57,58]. EIS was used to examine the effect of different PE shells of MCs applied as pH responsive components of smart coating for the anticorrosion protection of AA2024-T3.

The Bode plots of EIS after 1 h (a, b), 12 h (c, d), 24 h (e, f), 144 h (g, h), and 720 h (i, j) of immersion in 0.1 M NaCl for coated AA2024-T3 samples, with coatings modified with 2 wt% of BTA directly added, MC without PE shell and MCs having SPs and DPs of different PEs are presented in Fig. 6. The spectra can be divided into three frequency regions; high, intermediate and low f, which represents different parts of the samples [59], corresponding to electrochemical response of the coating, the native aluminium oxide layer and occurrence of corrosion on the metal substrate, respectively. Furthermore, with water-borne epoxy coating, early compromise of coating barrier properties enables the estimation of the effect of MCs, particularly, the influence of the shell in the active protection capabilities.

Clearly, direct addition of BTA into epoxy coating compromises the integrity of the coating as indicated by the lowest |Z| value for f-BTA from 12 h to 720 h of immersion. In addition, the phase angle plots for f-BTA obviously displays three time constants during 1 h of immersion suggesting early diffusion of electrolyte to the substrate and onset of

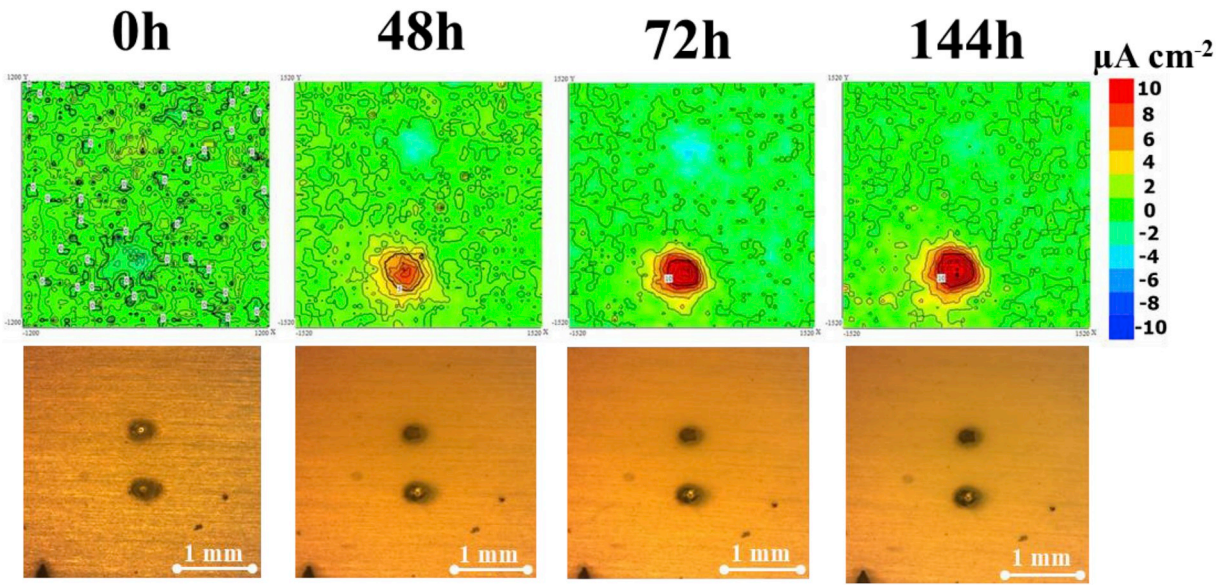

Fig. 8. SVET current density maps and photos of a defect on coated AA2024-T3 samples at different times of immersion in 0.05 M NaCl for reference coating. Scale units: μA cm^{-2}. Scanned area: ≈ 3.2 mm × 3.1 mm.

corrosion activity. The reference sample shows one time constant within 12 h, then two time constants from 24 h. The one time constant after 1 h and 12 h of immersion for the reference sample may be due to better passivation possibly as a result of more compact coating matrix in the absence of additives. Furthermore, the presence of MCs without PE shells (BTA@MSP) demonstrates similar poor protection. Conversely, MCs with PE shells seem to reveal overall consistency in maintaining coating properties. As seen in Fig. 6, MCs with PE shells show two time constants, with well depressed second time constant in the low frequency region throughout immersion time. After long immersion time of 720 h, coatings with PE-shelled MCs show higher impedance (see Fig. 6i). This can be attributed to active protection in the presence of MCs with PE shells.

To estimate the effect of nature and number of PE layers on the active protection, Fig. 7a gives a few indications. Fig. 7a presents evolution of lowest frequency impedance ($|Z|_{0.01Hz}$) from triplicate EIS measurements of coated AA2024-T3 samples. A decreasing trend of $|Z|_{0.01Hz}$ is observed for reference sample from 1 h to 720 h of immersion indicating a decline in the protective properties of coating. Furthermore, f-BTA displays the lowest $|Z|_{0.01Hz}$, corresponding to compromise of the barrier properties of coating upon direct addition of BTA. However, in the presence of MCs, better recoverability of coating with PE-shelled MCs can be observed. The rising trend of $|Z|_{0.01Hz}$ for BTA@MSP/PAH/PSS from 24 h to 720 h is obvious. As seen, BTA@MSP/PAH/PSS demonstrates the best recovery of coating properties, as indicated by highest $|Z|_{0.01Hz}$ after 720 h of immersion. Among the shelled MCs, it is interesting to observe that after 144 h of immersion, MCs with W-W PE shell (PEI/PAA or 2(PEI/PAA)) has slightly higher $|Z|_{0.01Hz}$ values when compared with their W-S PE shell (PAH/PSS or 2(PAH/PSS) counterparts. This is possibly due to the early availability of BTA which the W-W PE shell encourages as electrolyte permeates the coating. However, after 720 h, the samples with MC shells conferring more controlled release over time (PAH/PSS and 2(PAH/PSS) rises to higher $|Z|_{0.01Hz}$ values. Even so, the less thick layer (PAH/PSS) dominates. These observations with W-W PE shell (PEI/PAA or 2(PEI/PAA)) and W-S PE shell (PAH/PSS or 2(PAH/PSS) agree with the release patterns of PE-shelled MCs discussed earlier.

The EIS data of coated AA2024-T3 samples during 720 h of immersion in 0.1 M NaCl were fitted using the equivalent electrical circuit (EEC) shown in Fig. 7b–d, corresponding to one, two and three time constants, respectively. The EECs are overlaid in physical model that describes the electrochemical system. The physical meaning and phase response that describes the electrochemical process of the system and fit quality informed the choice of the EEC model. The EECs consist of the solution (electrolyte) resistance (R_{sol}), pore capacitance (C_{pore}), the pore resistance (R_{pore}), oxide layer capacitance (C_{ox}), resistance of the intermediate oxide layer (R_{ox}), double layer capacitance (C_{dl}) and charge transfer resistance (R_{ct}). In the circuit, constant phase element (CPE) is used for capacitance to accommodate the electrode heterogeneity of coated samples. The double-layer capacitance (CPE_{dl}) and the charge transfer resistance (R_{ct}) characterize the corrosion process and contribute to $|Z|$ values at low frequency [60]. The obtained fitting parameters are given in Tables 2 and 3. Clearly, f-BTA shows the lowest R_{pore} ($1.05 \times 10^6\ \Omega\ cm^2$) and R_{ox} ($2.86 \times 10^6\ \Omega\ cm^2$) values after 720 h. The reference sample also shows relatively low resistance values, with a clear decreasing trend of R_{ox}, which confirms no inhibition. Higher R_{pore} and R_{ox} values for coatings with MCs after 720 h validate their active protection and recovery capabilities. Moreover, MCs with W-S PE shell (PAH/PSS and 2(PAH/PSS) which recovers the coating back to one time constant show highest R_{pore} values; BTA@MSP/PAH/PSS ($8.64 \times 10^7\ \Omega\ cm^2$) and BTA@MSP/2(PAH/PSS) ($3.29 \times 10^7\ \Omega\ cm^2$).

Therefore, the coating with the overall highest R_{pore} after 720 h of immersion is BTA@MSP/PAH/PSS, with single pair shell of W-S PE shell. The performance of PAH/PSS and 2(PAH/PSS) could be due to their controlled pattern of inhibitor release, derivable from their strong linear structure in which the molecular PEMs interact strongly [51], but PAH/PSS performs better due to lesser thickness of PEMs. Overall, the EIS results show that although W-W PE shells encourage faster release of inhibitor, W-S PE shells lead to slower but more sustained release over time, recovering coating properties at longer immersion time of 720 h. Furthermore, SP shells support better active protection and recovery when compared to DP shells.

3.4. SVET analysis

Evaluation of active protection behaviour of BTA@MSP/PAH/PSS and BTA@MSP/PEI/PSS, was further carried out by scanning vibrating electrode technique (SVET). SVET allows the estimation and monitoring of corrosion activities in local environments of the substrate [61]. Corrosion activity producing anodic and cathodic currents on the surface of the AA2024-T3 substrate could involve anodic reactions: dissolution of the Al metal and its hydrolysis (Eq. (2) and (3), respectively)

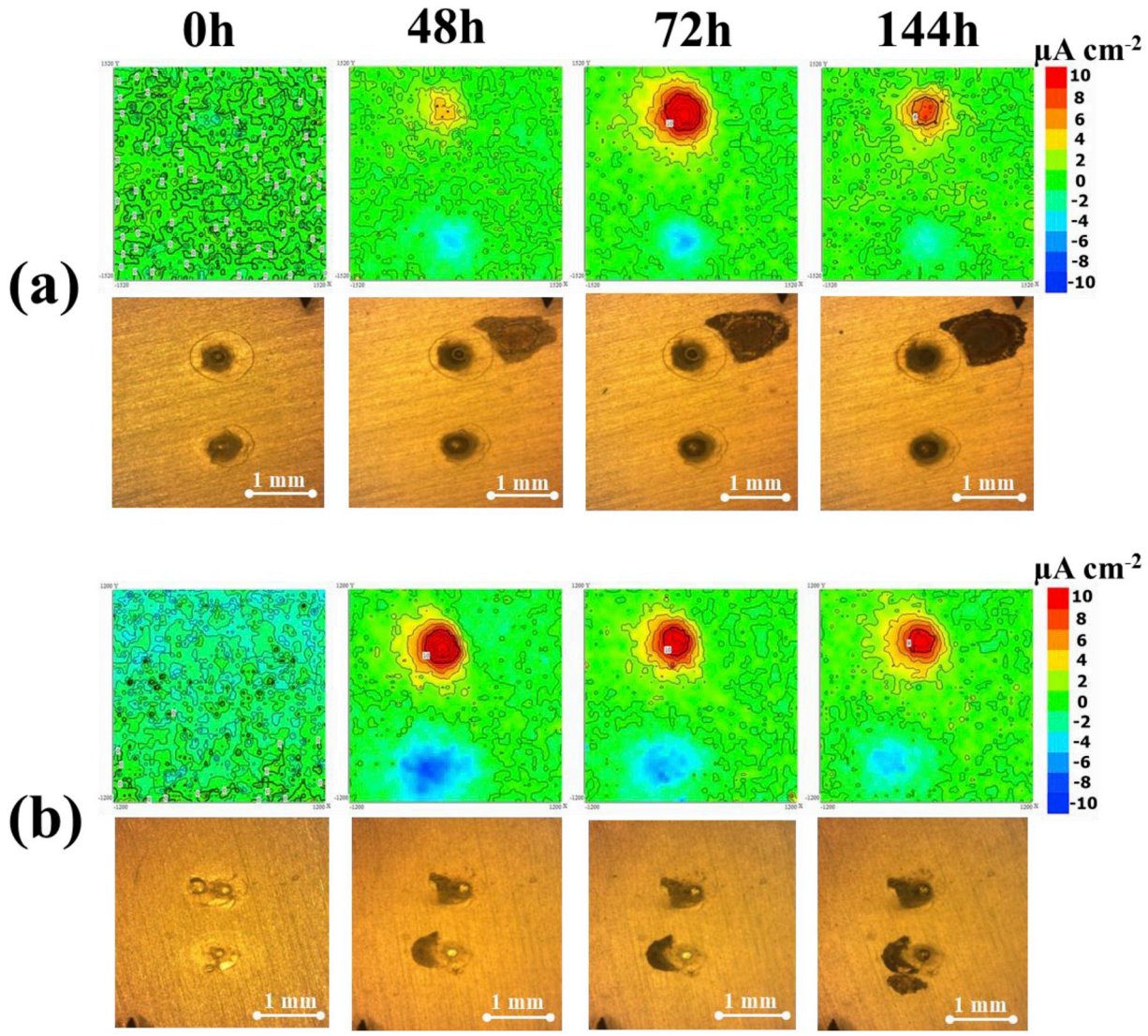

Fig. 9. SVET current density maps and photos of a defect on coated AA2024-T3 samples at different times of immersion in 0.05 M NaCl. Coating modified with 2 wt% microcontainers (a) BTA@MSP/PAH/PSS and (b) BTA@MSP/PEI/PAA. Scale units: μA cm^{-2}. Scanned area: ≈ 3.2 mm × 3.1 mm.

and dissolution of S-phase intermetallic Mg and its hydrolysis (Eq. (4) and (5), respectively) which lowers the local pH to around 3; and cathodic reactions: oxygen reduction and evolution of hydrogen (Eq. (6) and (7), respectively) which increases the local pH to around 10 [62,63].

$$Al \rightarrow Al^{3+} + 3e^- \quad (2)$$

$$Al^{3+} + nH_2O \rightarrow Al(OH)_n^{(3-n)} + nH^+, \quad n = 1-3 \quad (3)$$

$$Mg \rightarrow Mg^{2+} + 2e^- \quad (4)$$

$$Mg^{2+} + 2H_2O \leftrightarrow Mg(OH)_2 + 2H^+ \quad (5)$$

$$O_2 + 2H_2O + 4e^- \rightarrow 4OH^- \quad (6)$$

$$2H_2O + 2e^- \rightarrow 2OH^- + H_2 \quad (7)$$

The local pH gradients stimulate the permeability of containers leading to a release of inhibitors. The release of inhibitor stops with close of PE shell when pH reverts to initial value. Factors that affect pH gradients include the mechanism of corrosion, intermetallic inclusions, and surface properties of the substrate. With particular focus on intermetallic inclusions, Snihirova et al. reports that cathodic reactions that take place on S-phase intermetallic Cu leads to rise in local pH to 11.8 [61]. Anodic activity is assigned to dissolution of Mg. Both anodic and cathodic reactions occur on Al.

The SVET maps and photos of the area of the defect obtained after immersion of samples in 0.05 M NaCl are presented in Figs. 8–10. SVET maps and photos for reference sample are shown in Fig. 8. SVET maps and photos for coatings with 2 wt% BTA@MSP/PAH/PSS and BTA@MSP/PEI/PSS are depicted in Fig. 9 a and b, respectively. SVET maps and photos for coatings with 6 wt% BTA@MSP/PAH/PSS and BTA@MSP/PEI/PSS are shown in Fig. 10 a and b, respectively. Overall, little or no significant current is found at 0 h of immersion. The low insignificant currents observed outside the area of defect at 0 h may be due to background noise or early uptake of electrolyte. However, with the onset of corrosion activity over immersion time, samples show both anodic and cathodic currents after 48 h. The reference sample (Fig. 8) shows increasing current density (particularly anodic) in the defect area throughout the immersion time up to a maximum anodic current of 20.1 μA cm^{-2} at 144 h. This is due to increasing corrosion activity of the substrate in the defect area. In the presence of 2 wt% MCs (Fig. 9 a and b), there is initial increase in current density in the defect area from 48 h upon onset of corrosion activity. A decrease of current is noticed at 144 h, with maximum anodic currents of 9.1 μAcm^{-2} and 13.4 μAcm^{-2}

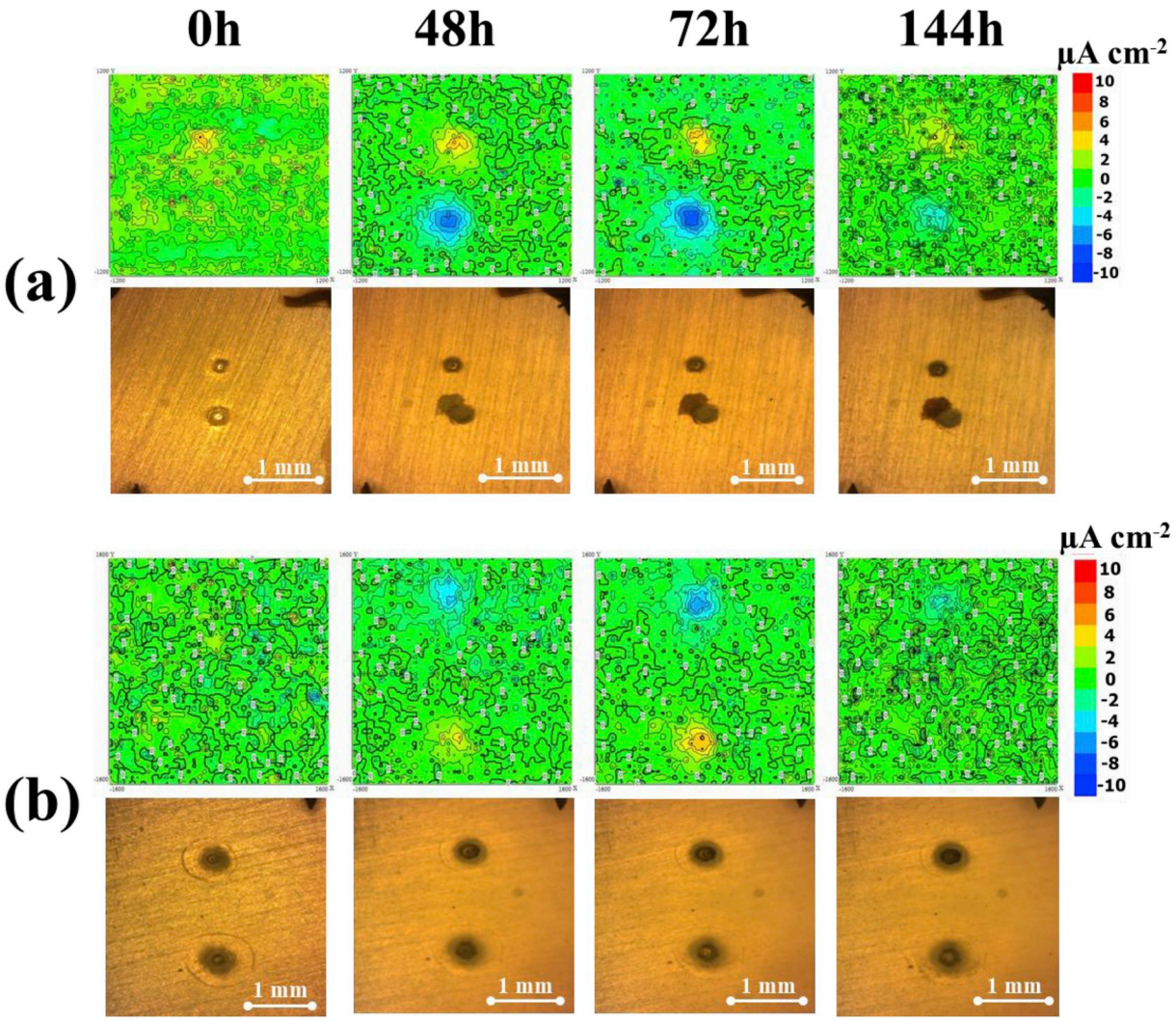

Fig. 10. SVET current density maps and photos of a defect on coated AA2024-T3 samples at different times of immersion in 0.05 M NaCl. Coating modified with 6 wt % microcontainers (a) BTA@MSP/PAH/PSS and (b) BTA@MSP/PEI/PAA. Scale units: μA cm^{-2}. Scanned area: ≈ 3.2 mm × 3.1 mm.

for BTA@MSP/PAH/PSS and BTA@MSP/PEI/PAA, respectively. This indicates the suppression of corrosion activity as a result of the active protection of the aluminium substrate by BTA released from MCs.

Coatings can provide passive and active protection. Considering, the SVET maps and photos in Fig. 8, the reference sample seems to provide no active protection as evidenced by increasing anodic and cathodic current, however the photos show coating that remains intact suggesting passivation. Fig. 9a and b demonstrates good active protection by the reduction of corrosion currents, however the detrimental effect of MC within coating matrix is evidenced by delamination in parts of the coating as shown by the photos. This suggests that the amount of BTA in 2 wt% MC may be insufficient to significantly counteract the detrimental effect. Therefore, with increase in the concentration of MCs to 6 wt% (Fig. 10), both passive and active protection is achieved. Maximum anodic current is as low as 4.5 μAcm^{-2} for BTA@MSP/PAH/PSS (see Fig. 10a) and almost no significant anodic current for BTA@MSP/PEI/PAA (see Fig. 10b). Clearly, from Fig. 10, 6 wt% of MCs demonstrates significant reduction in both anodic and cathodic currents and coatings remain intact compared with those of the samples containing 2 wt% containers, indicating better active and passive protection. In addition, it can be seen that with early BTA release from MC with W-W PE layers within 144 h, coating in Fig. 10b remains relatively more intact as indicated by the photos.

Moreover, in relationship to the shell, it is interesting to note the difference in Fig. 9 a and b. For W-S (PAH/PSS) shell there is delayed reduction in current density apparently due to initial slow release of BTA. As observed in Fig. 9a, between 48 h and 72 h, an increase in current is still observed. This may indicate that significant amount of BTA enough to begin the suppression of corrosion activity has not reached the corrosion site. Conversely, for W-W (PEI/PAA) shell (Fig. 9b), there is reduction in both anodic and cathodic currents from 48 h to 72 h, suggesting early availability of BTA. However, for both, active protection eventually takes place, as can be seen by the lower current density after 144 h. This observation supports faster release of BTA through W-W PE shell and confirms the observations in the release profile and EIS discussed in earlier sections. The agreement of the SVET and EIS results confirms the corrosion inhibition ability of BTA-loaded MCs, showing early inhibition for W-W PE shells.

3.5. Salt spray test

Salt spray test can indicate practical consequence of the application of self-healing components in smart coatings. Coatings were tested for their anticorrosion protection efficiency in the salt spray chamber after exposure for 120 h, photos of which are depicted in Fig. 11. The modification and optimization of MCs for improved barrier properties is currently on-going in our research group. Here, with water-borne epoxy coating and early degradation of coating, the effect of PE shells can be

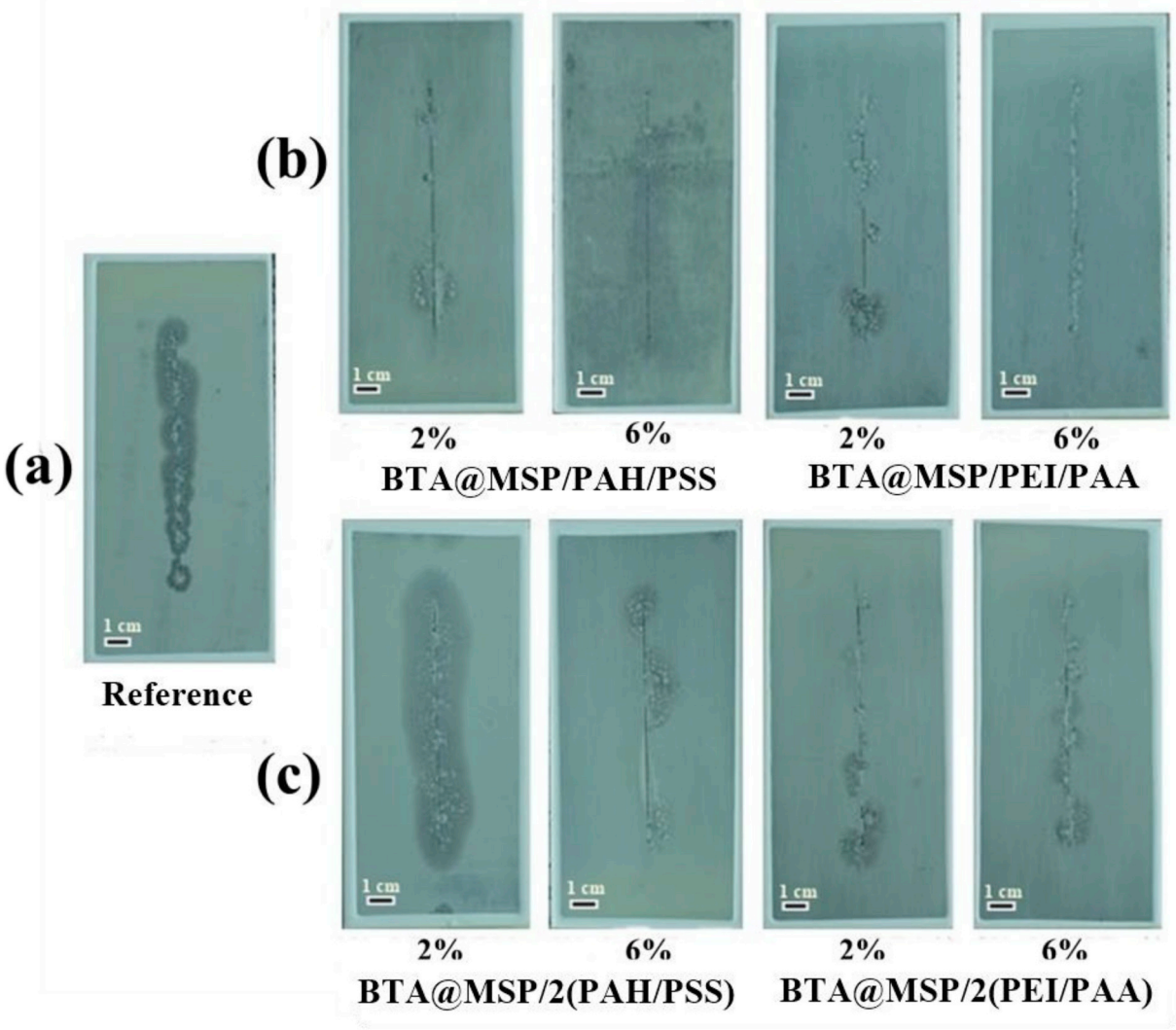

Fig. 11. Photos of coated samples with artificial scratch after exposure in salt spray chamber for 120 h: (a) reference; modified with microcontainers having (b) single pair polyelectrolyte shells, and (c) double pair polyelectrolyte shells.

estimated, which is our objective in this current work. Generally, more blisters in the area of the scratch indicate less protection against corrosion. Obvious blisters can be seen in the reference coating (Fig. 11a). Samples with MCs show protection of the scratch area, with better effect evident for samples with higher percentage of MCs (6%). However, samples with SP PE shell (Fig. 11b) show lesser blisters when compared with their DP counterparts (Fig. 11c). And because the availability of the inhibitor BTA is what informs the active protection, SPs with lesser shell thickness (as shown in Fig. 2) show better protection apparently due to more release of BTA. This observation is so in view of the pH-sensing ability of MCs in smart coatings. A slight change in pH occasioned by onset of corrosion when sensed by MCs can trigger more release of BTA through a less thick wall of PE shell. The consequence is easy and more availability of BTA in the samples with SP PE shell. Moreover, 2% 2(PEI/PAA) when compared with 2% 2(PAH/PSS) shows lesser blisters which means better active protection within a short time of experiment, which is in agreement with EIS result. The easier molecular transitions in PEMs made up of W-W PEs which allows easier passage of inhibitors through the PE "gates" may be responsible for the observation.

The response of PE shells of MCs to changes in pH is illustrated in Fig. 12a, leading to the release of BTA and active protection of artificial defect region as illustrated in Fig. 12b. The ability of PEs to open and close when triggered by changes in local pH arising from corrosion process is critical to pH-based active protection and is a significant factor in engineering active feedback systems for anticorrosion protection. Active protection based on pH thrives on the pH buffering ability of this PEs to pH gradients. The shell closes when pH reverts to neutral. As illustrated in Fig. 12b, corrosion activity on the defect site changes the local pH. The change in pH triggers the MCs, most likely in the neighbourhood of the defect, and the PE shells open in response. A release of BTA from MCs then activates protection of substrate in defect region. The mechanism of inhibition of AA2024-T3 corrosion by BTA is by forming complexes with copper, an alloying element, and described elsewhere [64]. However, significant role is played by the PE shells and their nature and number of layers is critical in the overall functionality of the coating. Furthermore, we recommend that further work can be carried out to examine whether the selected polyelectrolytes have inhibitive properties as well, and whether or not they contribute to corrosion inhibition within the system examined.

4. Conclusions

The influence of weak-strong and weak-weak polyelectrolyte shells on mesoporous silica particle-based microcontainers preloaded with BTA and applied as pH-sensitive component in smart coatings is reported in this paper. Successful fabrication of "smart" containers with weak-strong (PAH/PSS) and weak-weak (PEI/PAA) polyelectrolyte

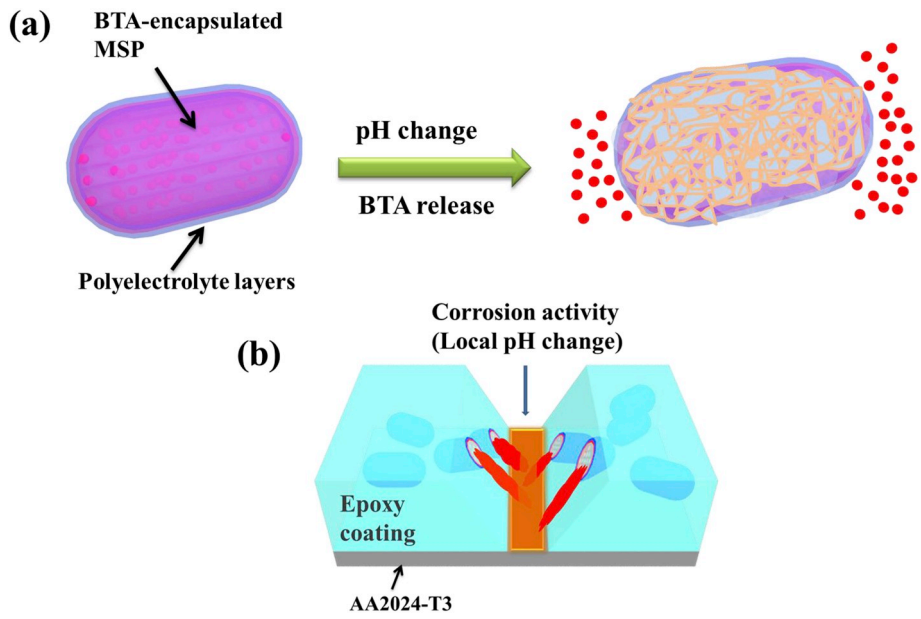

Fig. 12. Schematic illustrations: (a) response of polyelectrolyte shell to pH change leading to release of BTA, and (b) active response of epoxy coating modified with microcontainers to changes in pH at artificial defects.

shells aid active protection assessment, offering insight into the functionality of the coatings. FTIR and UV measurements confirm the encapsulation of BTA in the microcontainer. A 5.5% BTA encapsulation was revealed by UV measurements, corresponding to 66 mg g^{-1} of initial amount of mesoporous silica particles used. Successful deposition of polyelectrolyte shells was confirmed by zeta potential measurements and TEM.

Fabricated microcontainers are pH-sensitive and respond with a release of BTA upon change in pH. The self-release is higher in low and high pH values than in neutral pH, permitting active anticorrosion investigations. Slow and prolonged release is observed for microcontainers with PAH/PSS shell and quicker release pattern is noticed with PEI/PAA shell.

The active anticorrosion performance of microcontainers in smart coatings was demonstrated by EIS, SVET and salt spray tests. Polyelectrolyte shells of microcontainers were critical in the overall anticorrosion performance. Single pair shells showed better performance when compared with double pair shells. Furthermore, microcontainers with weak-weak polyelectrolyte shells showed immediate protection due to quicker response of the shell to pH changes. However, weak-strong polyelectrolyte shells led to slower but more controlled and prolonged release of inhibitor, resulting in better long term anticorrosion protection. The findings are critical and give insights in the choice of the nature of polyelectrolyte gatekeepers for designing feedback active systems, particularly in systems like smart coatings.

Data availability

The raw/processed data required to reproduce these findings cannot be shared at this time as the data also forms part of an ongoing study.

Declaration of competing interest

The authors declare that they have no known competing financial interests or personal relationships that could have appeared to influence the work reported in this paper.

Acknowledgements

The authors acknowledge the financial support from the National Natural Science Foundation of China (Grant numbers 51571202, 51001109).

References

[1] N.K. Rawat, S. Ahmad, Synergistic effect of nanosize and irradiation on epoxy/conducting poly(o-phenyldiamine) nanospheres composite coatings: synthesis, characterization and corrosion protective performance, Mater. Chem. Phys. 204 (2018) 282–293.
[2] M.L. Zheludkevich, J. Tedim, M.G.S. Ferreira, "Smart" coatings for active corrosion protection based on multi-functional micro and nanocontainers, Electrochim. Acta 82 (2012) 314–323.
[3] H. Elmsellem, H. Nacer, F. Halaimia, A. Aouniti, I. Lakehal, A. Chetouani, S. Al-Deyab, I. Warad, R. Touzani, B. Hammouti, Anti-corrosive properties and quantum chemical study of (E)-4-methoxy-N-(methoxybenzylidene)aniline and (E)-N-(4-methoxybenzylidene)-4-nitroaniline coating on mild steel in molar hydrochloric, Int. J. Electrochem. Sci. 9 (2014) 5328–5351.
[4] M.L. Zheludkevich, S.K. Poznyak, L.M. Rodrigues, D. Raps, T. Hack, L.F. Dick, T. Nunes, M.G.S. Ferreira, Active protection coatings with layered double hydroxide nanocontainers of corrosion inhibitor, Corros. Sci. 52 (2010) 602–611.
[5] D.G. Shchukin, M. Zheludkevich, K. Yasakau, S. Lamaka, M.G.S. Ferreira, H. Mohwald, Layer-by-layer assembled nanocontainers for self-healing corrosion protection, Adv. Mater. 18 (2006) 1672–1678.
[6] S.R.C. Arunchandran, R.P. George, U. Kamachi Mudali, Self-healing corrosion resistive coatings based on inhibitor loaded TiO_2 nanocontainers, J. Electrochem. Soc. 159 (2012) C552–C559.
[7] H. Elmsellem, Y.E. Ouadi, M. Mokhtari, H. Bendaif, H. Steli, A. Aouniti, A. Almehdi, I. Abdel-Rahman, H. Kusuma, B. Hammouti, A natural antioxidant and an environmentally friendly inhibitor of mild steel corrosion: a commercial oil of basil (Ocimum basilicum L.), J. Chem. Technol. Metall. 4 (2019) 742–749.
[8] M.G. Ahangari, A. Fereidoon, Micromechanical properties and morphologies of self-healing epoxy nanocomposites with microencapsulated healing agent, Mater. Chem. Phys. 151 (2015) 112–118.
[9] X. Liu, Y. Cheng, W. Wang, F. Liu, B. Hou, Application of 1D attapulgite as reservoir with benzotriazole for corrosion protection of carbon steel, Mater. Chem. Phys. 203 (2018) 292–302.
[10] Z.L. Zheng, M. Schenderlein, X. Huang, N.J. Brownball, F. Blanc, D. Shchukin, Influence of functionalization of nanocontainers on self-healing anticorrosive coatings, Acs Appl. Mater. Inter. 7 (2015) 22756–22766.
[11] Y. Wang, Y. Zhu, C. Li, D. Song, T. Zhang, X. Zheng, Y. Yan, M. Zhang, J. Wang, D. G. Shchukin, Smart epoxy coating containing Ce-MCM-22 zeolites for corrosion protection of Mg-Li alloy, Appl. Surf. Sci. 369 (2016) 384–389.
[12] M. Izadi, T. Shahrabi, B. Ramezanzadeh, Active corrosion protection performance of an epoxy coating applied on the mild steel modified with an eco-friendly sol-gel film impregnated with green corrosion inhibitor loaded nanocontainers, Appl. Surf. Sci. 440 (2018) 491–505.
[13] D. Snihirova, S.V. Lamaka, M.M. Cardoso, J.A.D. Condeco, H.E.C.S. Ferreira, M. D. Montemor, pH-sensitive polymeric particles with increased inhibitor-loading capacity as smart additives for corrosion protective coatings for AA2024, Electrochim. Acta 145 (2014) 123–131.

[14] M. Sun, A. Yerokhin, M.Y. Bychkova, D.V. Shtansky, E.A. Levashov, A. Matthews, Self-healing plasma electrolytic oxidation coatings doped with benzotriazole loaded halloysite nanotubes on AM50 magnesium alloy, Corros. Sci. 111 (2016) 753–769.
[15] D. Snihirova, S.V. Lamaka, M.F. Montemor, SMART" protective ability of water based epoxy coatings loaded with CaCO3 microbeads impregnated with corrosion inhibitors applied on AA2024 substrates, Electrochim. Acta 83 (2012) 439–447.
[16] D. Snihirova, S.V. Lamaka, M. Taryba, A.N. Salak, S. Kallip, M.L. Zheludkevich, M. G.S. Ferreira, M.F. Motemor, Hydroxyapatite microparticles as feedback-active reservoirs of corrosion inhibitors, Acs Appl. Mater. Inter. 2 (2010) 3011–3022.
[17] E. Alibakhshi, E. Ghasemi, M. Mandavian, B. Ramezanzadeh, A comparative study on corrosion inhibitive effect of nitrate and phosphate intercalated Zn-Al-layered double hydroxides (LDHs) nanocontainers incorporated into a hybrid silane layer and their effect on cathodic delamination of epoxy topcoat, Corros. Sci. 115 (2017) 159–174.
[18] X. Liu, C. Gu, Z. Ma, X. Ma, B. Hou, pH-responsive containers based on modified hollow TiO_2 for active and passive protection of carbon steel, J. Electrochem. Soc. 165 (2018) C145–C154.
[19] Y.M. Tang, Z.Y. Cao, J.Q. Xu, H. Cang, W.H. Jing, Titanate matrices as potential corrosion inhibitor nanocontainers, Corros. Sci. 88 (2014) 487–490.
[20] K.V. Yeole, I.P. Agarwal, S.T. Mhaske, The effect of carbon nanotubes loaded with 2-mercaptobenzothiazole in epoxy-based coatings, J. Coat. Technol. Res. 13 (2016) 31–40.
[21] A. Yabuki, T. Shiraiwa, I.W. Fathona, pH-controlled self-healing polymer coatings with cellulose nanofibers providing an effective release of corrosion inhibitor, Corros. Sci. 103 (2016) 117–123.
[22] I.A. Kartsonakis, A.C. Balaskas, G. Kordas, Influence of cerium molybdate containers on the corrosion performance of epoxy coated aluminium alloys 2024-T3, Corros. Sci. 53 (2011) 3771–3779.
[23] B.R.M. Gharagozlou, Z. Baradaran, Synthesize and characterization of a novel anticorrosive cobalt ferrite nanoparticles dispersed in silica matrix (CoFe2O4-SiO2) to improve the corrosion protection performance of epoxy coating, Appl. Surf. Sci. 377 (2016) 86–98.
[24] I.A. Kartsonakis, A.C. Balaskas, E.P. Koumoulos, C.A. Charitidis, G. Kordas, Incorporation of ceramic nanocontainers into epoxy coatings for the corrosion protection of hot dip galvanized steel, Corros. Sci. 57 (2012) 30–41.
[25] M. Kopec, K. Szczepanowicz, G. Mordarski, K. Podgorna, R.P. Socha, P. Nowak, P. Warszynski, T. Hack, Self-healing epoxy coatings loaded with inhibitor-containing polyelectrolyte nanocapsules, Prog. Org. Coat. 84 (2015) 97–106.
[26] J.M. Falcon, F.F. Batista, I.V. Aoki, Encapsulation of dodecylamine corrosion inhibitor on silica nanoparticles, Electrochim. Acta 124 (2014) 109–118.
[27] D.G. Shchukin, Container-based multifunctional self-healing polymer coatings, Polym. Chem. 4 (2013) 4871–4877.
[28] D.G. Shchukin, H. Mohwald, Smart nanocontainers as depot media for feedback active coatings, Chem. Commun. 47 (2011) 8730–8739.
[29] S.B. Ulaeto, R. Rajan, J.K. Pancrecious, T.P.D. Rajan, B.C. Pai, Developments in smart anticorrosive coatings with multifunctional characteristics, Prog. Org. Coat. 111 (2017) 294–314.
[30] S. Manasa, A. Jyothirmayi, T. Siva, B.V. Sarada, M. Ramakrishna, S. Sathiyanarayanan, K.V. Gobi, R. Subasri, Nanoclay-based self-healing, corrosion protection coatings on aluminum, A356.0 and AZ91 substrates, J. Coat. Technol. Res. 14 (2017) 1195–1208.
[31] T. Chen, J.J. Fu, An intelligent anticorrosion coating based on pH-responsive supramolecular nanocontainers, Nanotechnology 23 (2012) 505705.
[32] H.W. Shi, L.P. Wu, J. Wang, F.C. Liu, E.H. Han, Sub-micrometer mesoporous silica containers for active protective coatings on AA 2024-T3, Corros. Sci. 127 (2017) 230–239.
[33] D.G. Shchukin, H. Mohwald, Surface-engineered nanocontainers for entrapment of corrosion inhibitors, Adv. Funct. Mater. 17 (2007) 1451–1458.
[34] N.Y. Abu-Thabit, A.S. Hamdy, Stimuli-responsive Polyelectrolyte Multilayers for fabrication of self-healing coatings - a review, Surf. Coat. Technol. 303 (2016) 406–424.
[35] I.I. Udoh, H.W. Shi, F.C. Liu, E.H. Han, Synergistic effect of 3-Amino-1,2,4-triazole-5-thiol and cerium chloride on corrosion inhibition of AA2024-T3, J. Electrochem. Soc. 166 (2019) C185–C195.
[36] M.L. Zheludkevich, D.G. Shchukin, K.A. Yasakau, H. Mohwald, M.G.S. Ferreira, Anticorrosion coatings with self-healing effect based on nanocontainers impregnated with corrosion inhibitor, Chem. Mater. 19 (2007) 402–411.
[37] S. Marcelin, N. Pebere, Synergistic effect between 8-hydroxyquinoline and benzotriazole for the corrosion protection of 2024 aluminium alloy: a local electrochemical impedance approach, Corros. Sci. 101 (2015) 66–74.
[38] I. Recloux, M. Mouanga, M.E. Druart, Y. Paint, M.G. Olivier, Silica mesoporous thin films as containers for benzotriazole for corrosion protection of 2024 aluminium alloys, Appl. Surf. Sci. 346 (2015) 124–133.
[39] Y. Feng, Y.F. Cheng, An intelligent coating doped with inhibitor-encapsulated nanocontainers for corrosion protection of pipeline steel, Chem. Eng. J. 315 (2017) 537–551.
[40] F. Maia, J. Tedim, A.D. Lisenkov, A.N. Salak, M.L. Zheludkevich, M.G.S. Ferreira, Silica nanocontainers for active corrosion protection, Nanoscale 4 (2012) 1287–1298.
[41] A.C. Balaskas, M. Curioni, G.E. Thompson, Effectiveness of 2-mercaptobenzothiazole, 8-hydroxyquinoline and benzotriazole as corrosion inhibitors on AA 2024-T3 assessed by electrochemical methods, Surf. Interface Anal. 47 (2015) 1029–1039.
[42] Y.Y. Wang, P.J. Burke, Polyelectrolyte multilayer electrostatic gating of graphene field-effect transistors, Nano Res. 7 (2014) 1650–1658.
[43] E. Yoshida, Self-assembly of poly(allylamine hydrochloride) through electrostatic interaction with sodium dodecyl sulfate, Colloid Polym. Sci. 288 (2010) 1321–1325.
[44] S.M. Notley, Adsorption of polyelectrolyte modified graphene to silica surfaces: Monolayers and multilayers, J. Colloid Interface Sci. 375 (2012) 35–40.
[45] P. Overton, E. Danilovtseva, E. Karjalainen, M. Karesoja, V. Annenkov, H. Tenhu, V. Aseyev, Water-dispersible silica-polyelectrolyte nanocomposites prepared via acid-triggered polycondensation of silicic acid and directed by polycations, Polymers 8 (2016) 96–114.
[46] H.L. Guo, Q.Q. Guo, T.C. Chu, X.G. Zhang, Z.M. Wu, D.M. Yu, Glucose-sensitive polyelectrolyte nanocapsules based on layer-by-layer technique for protein drug delivery, J. Mater. Sci. Mater. Med. 25 (2014) 121–129.
[47] A. Khajouei, E. Jamalizadeh, S.M.A. Hosseini, Corrosion protection of coatings doped with inhibitor-loaded nanocapsules, Anti-corrosion Methods & Mater. 62 (2015) 88–94.
[48] S.G. Aziz, S.A. Elroby, A. Alyoubi, O.I. Osman, R. Hilal, Experimental and theoretical assignment of the vibrational spectra of triazoles and benzotriazoles. Identification of IR marker bands and electric response properties, J. Mol. Model. 20 (2014) 78–92.
[49] D. Fix, D.V. Andreeva, Y.M. Lvov, D.G. Shchukin, H. Mohwald, Application of inhibitor-loaded halloysite nanotubes in active anti-corrosive coatings, Adv. Funct. Mater. 19 (2009) 1720–1727.
[50] F.D. Simon, E.S. Dragan, F. Bucatariu, Reactive polyelectrolyte multilayers unto silica particles, React. Funct. Polym. 68 (2008) 1178–1184.
[51] L. Seon, P. Lavalle, P. Schaaf, F. Boulmedais, Polyelectrolyte multi layers: a versatile tool for preparing antimicrobial coatings, Langmuir 31 (2015) 12856–12872.
[52] P. Lavalle, C. Gergely, F.J.G. Cuisinier, G. Decher, P. Schaaf, J.C. Voegel, C. Picart, Comparison of the structure of polyelectrolyte multilayer films exhibiting a linear and an exponential growth regime: an in situ atomic force microscopy study, Macromolecules 35 (2002) 4458–4465.
[53] N. Laugel, C. Betscha, M. Winterhalter, J.C. Voegel, P. Schaaf, V. Ball, Relationship between the growth regime of polyelectrolyte multilayers and the polyanion/polycation complexation enthalpy, J. Phys. Chem. B 110 (2006) 19443–19449.
[54] G. Decher, Fuzzy nanoassemblies: toward layered polymeric multicomposites, Science 277 (1997) 1232–1237.
[55] L. Richert, A.J. Engler, D.E. Discher, C. Picart, Elasticity of native and cross-linked polyelectrolyte multilayer films, Biomacromolecules 5 (2004) 1908–1916.
[56] D.O. Grigoriev, K. Kohler, E. Skorb, D.G. Shchukin, H. Mohwald, Polyelectrolyte complexes as a "smart'' depot for self-healing anticorrosion coatings, Soft Matter 5 (2009) 1426–1432.
[57] D. Borisova, H. Mohwald, D.G. Shchukin, Influence of embedded nanocontainers on the efficiency of active anticorrosive coatings for aluminum alloys Part I: influence of nanocontainer concentration, Acs Appl. Mater. Inter. 4 (2012) 2931–2939.
[58] A. Lutz, O. van den Berg, J. Van Damme, K. Verheyen, E. Bauters, I. De Graeve, F. E. Du Prez, H. Terryn, A shape-recovery polymer coating for the corrosion protection of metallic surfaces, Acs Appl. Mater. Inter. 7 (2015) 175–183.
[59] D. Borisova, D. Akcakayiran, M. Schenderlein, H. Mohwald, D.G. Shchukin, Nanocontainer-based anticorrosive coatings: effect of the container size on the self-healing performance, Adv. Funct. Mater. 23 (2013) 3799–3812.
[60] D. Snihirova, S.V. Lamaka, P. Taheri, J.M.C. Mol, M.F. Montemor, Comparison of the synergistic effects of inhibitor mixtures tailored for enhanced corrosion protection of bare and coated AA2024-T3, Surf. Coat. Technol. 303 (2016) 342–351.
[61] D. Snihirova, M. Taryba, S.V. Lamaka, M.F. Montemor, Corrosion inhibition synergies on a model Al-Cu-Mg, sample studied by localized scanning electrochemical techniques, Corros. Sci. 112 (2016) 408–417.
[62] S.V. Lamaka, D.G. Shchukin, D.V. Andreeva, M.L. Zheludkevich, H. Mohwald, M.G. S. Ferreira, Sol-Gel/polyelectrolyte active corrosion protection system, Adv. Funct. Mater. 18 (2008) 3137–3147.
[63] H.B. Ding, L.H. Hihara, Localized corrosion currents and pH profile over B_4C, SiC, and Al_2O_3 reinforced 6092 aluminum composites - I. In 0.5 m Na_2SO_4 solution, J. Electrochem. Soc. 152 (2005) B161–B167.
[64] G. Williams, A.J. Coleman, H.N. McMurray, Inhibition of Aluminium Alloy AA2024-T3 pitting corrosion by copper complexing compounds, Electrochim. Acta 55 (2010) 5947–5958.